

The IACOB project[★]

VI. On the elusive detection of massive O-type stars close to the ZAMS

G. Holgado^{1,2,3}, S. Simón-Díaz^{2,3}, L. Haemmerlé⁴, D. J. Lennon^{2,3}, R. H. Barbá⁵, M. Cerviño¹, N. Castro⁶,
A. Herrero^{2,3}, G. Meynet⁴, J. I. Arias⁵

¹ Centro de Astrobiología, ESAC campus, Villanueva de la Cañada, E-28 692, Spain

² Instituto de Astrofísica de Canarias, E-38200 La Laguna, Tenerife, Spain.

³ Departamento de Astrofísica, Universidad de La Laguna, E-38205 La Laguna, Tenerife, Spain.

⁴ Département d'Astronomie, Université de Genève, chemin des Maillettes 51, CH-1290 Versoix, Switzerland

⁵ Departamento de Física y Astronomía, Universidad de La Serena, Avenida Juan Cisternas 1200, La Serena, Chile.

⁶ Leibniz-Institut für Astrophysik Potsdam (AIP), An der Sternwarte 16, 14 482 Potsdam, Germany

July 7, 2020

ABSTRACT

Context. The apparent lack of massive O-type stars near the zero-age main sequence, or ZAMS (at ages < 2 Myr), is a topic that has been widely discussed in the past 40 years. Different explanations for the elusive detection of these young massive stars have been proposed from the observational and theoretical side, but no firm conclusions have been reached yet.

Aims. We reassess this empirical result here, benefiting from the high-quality spectroscopic observations of (more than 400) Galactic O-type stars gathered by the IACOB and OWN surveys.

Methods. We used effective temperatures and surface gravities resulting from a homogeneous semi-automatized IACOB-GBAT/FASTWIND spectroscopic analysis to locate our sample of stars in the Kiel and spectroscopic Hertzsprung-Russell (sHR) diagrams. We evaluated the completeness of our magnitude-limited sample of stars as well as potential observational biases affecting the compiled sample using information from the Galactic O star catalog (GOSC). We discuss limitations and possible systematics of our analysis method, and compare our results with other recent studies using smaller samples of Galactic O-type stars. We mainly base our discussion on the distribution of stars in the sHR diagram in order to avoid the use of still uncertain distances to most of the stars in our sample. However, we also performed a more detailed study of the young cluster Trumpler-14 as an illustrative example of how *Gaia* cluster distances can help to construct the associated classical HR diagram.

Results. We find that the apparent lack of massive O-type stars near the ZAMS with initial evolutionary masses in the range between ≈ 30 and $70 M_{\odot}$ still persist even when spectroscopic results from a large non-biased sample of stars are used. We do not find any correlation between the dearth of stars close to the ZAMS and obvious observational biases, limitations of our analysis method, and/or the use of one example spectroscopic HR diagram instead of the classical HR diagram. Finally, by investigating the effect of the efficiency of mass accretion during the formation process of massive stars, we conclude that an adjustment of the mass accretion rate towards lower values than canonically assumed might reconcile the hotter boundary of the empirical distribution of optically detected O-type stars in the spectroscopic HR diagram and the theoretical birthline for stars with masses above $\approx 30 M_{\odot}$. Last, we also discuss how the presence of a small sample of O2–O3.5 stars found much closer to the ZAMS than the main distribution of Galactic O-type star might be explained in the context of this scenario when the effect of nonstandard star evolution (e.g. binary interaction, mergers, and/or homogeneous evolution) is taken into account.

Key words. Stars: early-type – Stars: massive – Stars: Hertzsprung-Russell diagram – Stars: evolution – Stars: formation – Techniques: spectroscopic

1. Introduction

A fundamental phase in stellar evolution is the instant of nuclear ignition of hydrogen in the core of the newly formed star. This point in the Hertzsprung-Russell (HR) diagram is commonly known as the zero-age main sequence (ZAMS) and indicates both the beginning of the main sequence (MS) and the theoretical boundary between the star formation process and its further evolution. Another important concept in this context is the so-called birthline, which represents the path followed by a star in formation along the HR diagram until the accreting material is

exhausted or until the associated parental cloud is dissolved and the star becomes observable in the optical. The properties of this birthline critically depend on the mass accretion rate during the formation of the star (Bernasconi & Maeder 1996; Norberg & Maeder 2000; Haemmerlé et al. 2019).

If accretion stops before the star has reached the ZAMS, that is, the Kelvin-Helmholtz (KH) timescale of the proto-star is longer than its accretion timescale (as is the case of intermediate- and low-mass stars; Larson 1969, 1972; Stahler 1983), further evolution of the proto-stellar object until it reaches the ZAMS coincides with a classical KH contraction at constant mass, and is well described by canonical non-accreting models (Siess et al. 1997; Baraffe et al. 2009, 2012; Hosokawa et al. 2011; Tognelli et al. 2015). In this case, the lower envelope of the birthline is

Send offprint requests to: gholgado@cab.inta-csic.es

[★] Table E.1 is available in electronic form at the CDS via <http://cdsarc.u-strasbg.fr/viz-bin/cat/J/A+A/638/A157>

delineated by the observable low- and intermediate-mass young pre-MS stellar objects, including Herbig AeBe stars, and different types of T Tauri stars (e.g., Stahler 1988; Palla & Stahler 1990, 1992; Norberg & Maeder 2000; Behrend & Maeder 2001; Haemmerlé et al. 2019).

If, in contrast, nuclear burning of hydrogen starts before accretion is complete (as is the case of stars above a certain mass, see, e.g., Haemmerlé et al. 2019), the star will already have evolved away from the ZAMS when it emerges from the parental cloud. As a consequence, the birthline is expected to delimit a lower envelope (hotter stars) of massive MS stars that are observable in the optical. In this case, when accretion stops and the star has reached its maximum mass, it leaves the birthline to follow the canonical mass evolution toward lower effective temperatures. How close the birthline of massive stars is to the ZAMS depends on the considered accretion rate (Bernasconi & Maeder 1996; Vanbeveren et al. 1998; Norberg & Maeder 2000; Behrend & Maeder 2001; Hosokawa & Omukai 2009; Hosokawa et al. 2010; Haemmerlé et al. 2016, 2019).

Stars with masses above $\sim 15 M_{\odot}$ are characterized by having O spectral types during their MS phase. Because they evolve rapidly (stars with more than $\sim 40 M_{\odot}$ leave the MS in less than 4 Myr; see Brott et al. 2011; Ekström et al. 2012, although this strongly depends on specific mass-loss rates), the presence of O-type stars in a galactic region normally indicates a recent (or still active) star formation event (Herbig 1962). The short nuclear burning timescale characterizing these stars, which is comparable with the timescale required to dissolve the associated parental cloud, was originally proposed to be the reason of the apparent lack of Galactic O-type stars close to the theoretical ZAMS (Garmany et al. 1982). Other related explanations for this gap in the upper left part of the HR diagram have been put forward. One of these is the occurrence of observational biases caused by the lack of stars from really young clusters ($< 1-2$ Myr) in the investigated samples (Herrero et al. 2007) and/or the fact that young massive stars, being still embedded in their birth cocoon, are heavily reddened and hence easily elude magnitude-limited samples (Yorke 1986; Hanson 1998). However, another interesting possibility has not yet been investigated in detail (in spite of former approaches, e.g., Herrero et al. 2007): that the empirical hot boundary of O-type stars detected in the optical might correspond to a stellar birthline of massive stars associated with a lower accretion rate than canonically assumed (see, e.g., Vanbeveren et al. 1998).

The elusive detection of massive stars with mid-O spectral types (i.e., with masses in the range $\sim 30-60 M_{\odot}$) close to the ZAMS has been a persistent empirical result since the pioneering work on the Milky Way by Garmany et al. (1982). This peculiar empirical feature was also shown to be present (although not in a completely conclusive way) in other galaxies of the Local Group in Massey & Johnson (1993), Massey et al. (1995a), and Massey et al. (1995b). These authors, who investigated the massive star population of the Magellanic Clouds, NGC 6822, M 31 and M 33, also found that in the case of the Magellanic Clouds, their reddening data rendered the suggestion unlikely that such an absence (if real) would be due to the length of time that it takes a massive star to emerge.

Although the above-mentioned studies based the determination of effective temperatures (T_{eff}) and absolute magnitudes (M_v) of their large samples on standard (by that time) M_v , bolometric correction (B.C), T_{eff} calibrations (Morton 1969; Conti 1975), and distance modulus given in the literature (e.g., Humphreys 1978), similar results were later obtained by different authors using medium-size samples of O-type stars that

were investigated spectroscopically, both in the Milky Way (Herrero et al. 1992, 2007; Repolust et al. 2004; Castro et al. 2014; Holgado et al. 2018) and the Large Magellanic Cloud (Sabín-Sanjulián et al. 2017).

In this work, we benefit from (1) the observational efforts devoted in the past decade by the Galactic O Star Spectroscopic Survey (GOSSS, Maíz Apellániz et al. 2011) and the high-resolution spectroscopic surveys IACOB and OWN (last described in Simón-Díaz et al. 2015a; Barbá et al. 2017, respectively), and (2) the availability of stellar atmosphere codes that incorporate the most important physical processes in the modeling of O-type stars (such as the code used in this work, FASTWIND; Santolaya-Rey et al. 1997; Puls et al. 2005) to reassess this intriguing and still unresolved empirical result.

The structure of this paper is as follows. The observations and characteristics of the sample are described in Sect. 2. Sections 3 and 4 briefly present the method and results associated with the quantitative spectroscopic analysis of the likely single and single-line spectroscopic binaries in our sample, respectively. In Section 5 we evaluate potential observational biases and analysis limitations that might affect our results and might explain the non-detection of O-type stars close to the ZAMS, and we examine possible physical explanations for the existence of this gap. Concluding remarks and ideas for further investigation are presented in Sect. 6.

2. Observations and characteristics of the sample

The observations used for this study came from the two recent spectroscopic surveys IACOB and OWN. IACOB is a long-term observational project started in 2008 motivated by the compilation and scientific exploitation of a large database of high-resolution multi-epoch spectra of Galactic OB stars. While this project initially concentrated on stars observable from the Roque de los Muchachos observatory (La Palma, Spain), that is, the Northern Hemisphere, in 2012 we established a collaboration with the (also long-term) complementary OWN survey. The latter, started in 2005, pursues a long-term high-resolution monitoring of Southern Galactic O- and WN-type stars. In particular, and for the sake of homogeneity with the spectroscopic observations compiled in the framework of the IACOB project (comprising spectra obtained with the FIES at the NOT2.56m and HERMES at the Mercator1.2m spectrographs), we mainly concentrate on the spectra gathered by the OWN project using the FEROS instrument (attached to MPG/ESO-2.2m).

As described in Holgado et al. (2017, 2018), the combined efforts of the two surveys have resulted in a high-quality ($R > 25\,000$, signal-to-noise ratio, $S/N > 100$) database of ~ 2900 spectra of more than 400 Galactic O-type stars. All these stars are included in version 4.1 of the Galactic O-star catalog (GOSC, Maíz Apellániz et al. 2013), from which we also extracted other information of interest for this study, such as spectral classifications, data on photometry and extinction, and some notes on confirmed spectroscopic binarity. We also use GOSC to evaluate the completeness of our sample. In this context, we note that the version of GOSC we used as reference is considered to be complete up to $B=8$. Furthermore, it extends to objects as faint as $B=16$ with a decreasing level of completeness with respect to the expected number of stars per magnitude bin (see Figs. 7 and 4 in Maíz Apellániz et al. 2013, 2016, respectively). For example, while the catalog is predicted to be $\sim 95\%$ complete for stars with a B -magnitude in the range $8-9$ mag, this percentage drops to $\sim 50\%$ in the $9-10$ mag bin (see below and Sect. 5.1).

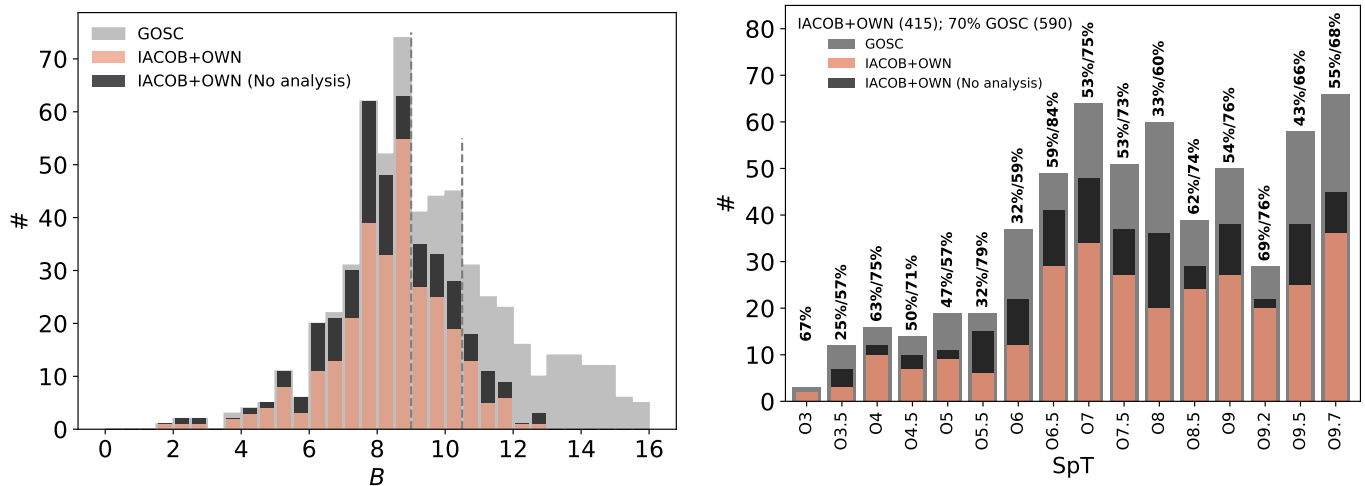


Fig. 1: Comparison of our working sample of Galactic O-type stars (pink and black) to the complete list of stars of this type included in v4.1 of GOSC (gray). We separate in the two panels the stars for which we have been able to obtain spectroscopic parameters (pink) and those for which we did not perform any quantitative spectroscopic analysis. These last stars are not considered hereinafter (black). *Left* Histogram of stars with respect to the B -magnitude. The vertical dashed lines mark the 90 and 80% completeness limits in our sample using GOSC as reference. *Right* Number of stars per spectral type. Percentages indicate the respective completeness of stars marked in pink and black, in the bottom and top panels, respectively, with respect to GOSC.

As shown in Fig. 1, our initial working sample includes 415 Galactic O-type stars covering a range in B -magnitude between ≈ 2 and 12.5, and spectral types (SpT) between O3 and O9.7 (left and right panels, respectively). We note, however, that not all stars in this initial sample were used for this study. We concentrate on the 285 stars for which we were able to perform a quantitative spectroscopic analysis (i.e. mainly the likely single stars and the single-line spectroscopic binaries, SB1), and excluded stars that are identified as double-line spectroscopic binaries (SB2) and/or that have strong spectroscopic evidence of being Oe or magnetic stars.

As illustrated in the left panel of Fig. 1, the IACOB+OWN sample comprises more than 90% of the stars with $B \leq 9$ mag quoted in version 4.1 of GOSC and includes a large portion ($\sim 70\%$) of the stars in this catalog with B magnitudes in the range 9–10.5 mag. The situation becomes more critical for fainter stars; this is a natural consequence of the observational limitations of the IACOB and OWN surveys. We note that the fainter tail of the B -magnitude distribution of stars in GOSC is built using spectra compiled in the framework of the intermediate-resolution ($R = 2\,500$) survey GOSSS, which is able to cover a wider range in apparent B -magnitude than the IACOB and OWN surveys.

The right panel of Fig. 1 shows the distribution of our working sample by spectral type, again including a comparison with the stars in GOSC. The figure also indicates for each spectral type the number and percentage of stars for which we were able to obtain spectroscopic parameters, separating them from those for which we did not perform the quantitative spectroscopic analysis (most of them are SB2). We have high-resolution spectra for ~ 60 – 80% of the stars in GOSC for each spectral type bin in the histogram, although about 10–30% of them belong to the sample of stars for which we did not obtain spectroscopic parameters. Overall, there seems to be no great difference between the distribution of spectral types in the two samples; this indicates that our working sample can be considered a good representation of all Galactic O-type stars comprising version 4.1 of GOSC.

3. Methods

While we here only discuss the stellar effective temperature (T_{eff}) and surface gravity ($\log g$) of our sample, we note that this is only a small subset of parameters that we determined using current methods. The full list of results, including parameters such as projected rotational velocity ($v \sin i$), surface abundances, microturbulence, and the wind parameters that can be determined from the quantitative spectroscopic analysis of the optical spectrum of a O-type stars, will be presented in a forthcoming paper.

We refer to Holgado et al. (2018) for a detailed description of our analysis method, with additional details and examples provided in Sabín-Sanjulián et al. (2014, 2017) and Simón-Díaz et al. (2017). In brief, in a first step all the multi-epoch spectra of a given star (we count at least three epochs for 70% of the stars) are used to provide a first classification in terms of spectroscopic variability (due to, e.g., binarity, pulsations, wind-variability and/or other sources of stellar variability). Then, the spectrum with the best S/N for each star (considering only likely single or single-line spectroscopic binaries, SB1) is used for the quantitative spectroscopic analysis. The latter is performed by means of two semi-automatized tools designed in the framework of the IACOB project, IACOB-BROAD (Simón-Díaz & Herrero 2014) and IACOB-GBAT (Simón-Díaz et al. 2011). These two together allow determining the line-broadening and spectroscopic parameters as well as the associated uncertainties of large samples of O-type stars in a homogeneous, objective, and relatively fast way.

The IACOB-BROAD analysis is based on the application of a combined Fourier transform (FT) plus goodness-of-fit (GOF) technique to an isolated line profile. For the sample under study, we used $O\text{ III } \lambda 5592$ as the main diagnostic line, although in a few cases (very fast rotators), we needed to rely on He I or He II lines. IACOB-BROAD then provides estimates for the projected rotational velocity ($v \sin i$) and the amount of macroturbulent broadening (v_{mac}).

The remaining spectroscopic parameters, T_{eff} , $\log g$, Y_{He} , ξ_t (microturbulence), β (the exponent of the wind velocity law¹), $\log Q$ (wind-strength parameter²), are obtained with IACOB-GBAT. This grid-based automatic tool, which is optimized for the quantitative spectroscopic analysis of O-type stars, performs an optimized χ^2 line-profile fitting of a set of H I and He I-II strategic diagnostic lines (see e.g., Holgado et al. 2018) using synthetic profiles associated with a vast grid of FASTWIND models (Santolaya-Rey et al. 1997; Puls et al. 2005; Rivero González et al. 2012). As indicated above, for this study, we only retained two of the resulting parameters from the IACOB-GBAT analysis: the effective temperature (T_{eff}), and surface gravity ($\log g$). The latter was combined with the derived $v \sin i$ to compute the surface gravity corrected for centrifugal acceleration ($\log g_{\text{true}}$, where $g_{\text{true}} = g + g_{\text{cent}}$, see Repolust et al. 2004)³.

Figure 2 shows the coverage in the spectroscopic HR diagram (sHRD, Langer & Kudritzki 2014) of the grid of FASTWIND models that is incorporated in IACOB-GBAT. This HR-analogous diagram was constructed by combining the T_{eff} and $\log g_{\text{true}}$ spectroscopic parameters into the \mathcal{L} parameter, which is equivalent to the L/M ratio as $\mathcal{L} := T_{\text{eff}}^4/g_{\text{true}} \sim L/M$, establishing a useful diagram to compare observations and evolutionary models regardless of distance and extinction constraints (see Sect. 4). The figure also depicts for reference the ZAMS, the evolutionary tracks, and several isochrones resulting from the nonrotating solar metallicity Geneva models (Ekström et al. 2012; Georgy et al. 2013). Our FASTWIND grid properly covers the full MS for stars with masses in the range 20–85 M_{\odot} .

This figure also serves to illustrate a limitation of our analysis strategy. For very hot stars, the He I lines become very weak or disappear (see the bottom left panel in Figure 2). This hampers an accurate determination of T_{eff} based on the He I and He II ionization balance. This situation means that the results from IACOB-GBAT in the region of the sHRD that is marked with crosses (and delimited by the diagonal line) are less reliable than for cooler O-type star in our sample. As we show in Sect. 4, the problematic stars are mainly those with spectral types earlier than O4. An alternative analysis using the N IV and N V lines (see, e.g., Rivero González et al. 2012) would be better suited to achieve a more accurate determination of T_{eff} (and hence $\log g$) for these early O-type stars. A complete and detailed HHeN analysis of all O-type stars in the IACOB+OWN sample is planned for a future paper; however, as a sanity check and for the purposes of this paper, we performed a preliminary analysis of the sample of early O-type star using part of the HHeN grid that we are currently computing at the IAC. As a result, we found differences in T_{eff} not larger than 2000 K in several stars, and 1000 K in the rest. This is in part thanks to the availability of the He I $\lambda 5875$ line in the IACOB-GBAT analyses, which remains strong enough at higher effective temperatures than the other He I lines in the blue region of the spectra.

In this analysis we avoided combining the outcome from our quantitative spectroscopic analysis with data on distances resulting from the parallaxes provided by *Gaia*-DR2 (Gaia Collaboration et al. 2018a). While *Gaia*-DR2 data are proving to be of great help to derive more accurate estimates of distances to clusters and associations that include massive stars (Berlanas et al. 2019; Drew et al. 2018, 2019; Davies & Beasar 2019), the use of individual parallaxes for most of our sample of O-type stars

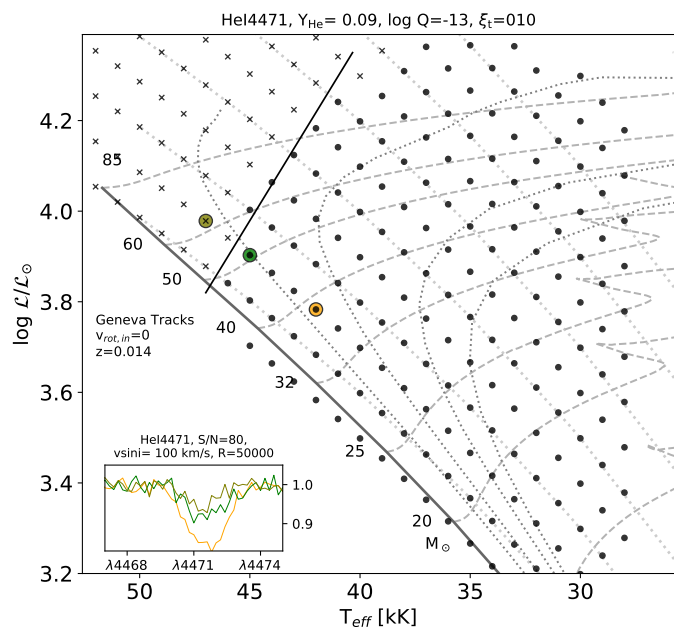


Fig. 2: Coverage of our grid of FASTWIND models in the sHRD (Langer & Kudritzki 2014). The evolutionary tracks (dashed), location of the ZAMS (solid gray), and isochrones (dotted) for $\tau = 1, 2, 3$, and 4 Myr as resulting from the nonrotating solar metallicity models by Ekström et al. (2012) and Georgy et al. (2013) are shown for reference. The dotted diagonal lines (following the points) are isocontours of constant gravity. Crosses map models with $EW(\text{He I } \lambda 4471) < 0.15 \text{ \AA}$. The solid black line separates these models from those for which the He I $\lambda 4471$ line has a larger EW (represented by dots). The inset in the bottom left corner depicts three He I $\lambda 4471$ line profiles corresponding to the models highlighted in the figure with large colored circles (see text for details of the analysis).

is still problematic because some still limiting systematic errors remain (e.g., calibration limitations for bright stars and under-sampling, see Lindegren et al. 2018; Arenou et al. 2018; Luri et al. 2018). In particular, we note that the parallax distribution of our sample is strongly peaked around 0.3–0.4 mas, with a median value of ~ 0.4 mas. This should be compared with typical parallax uncertainties of 0.03–0.04 mas (see Fig. A.1), and with the position-dependent zero-point uncertainty in the range 0.03–0.08 mas (see the discussion of Davies & Beasar (2019)). We therefore limit our study to the investigation of the distribution of O-type stars in the spectroscopic HR diagram and defer a discussion of individual parallaxes after publication of *Gaia*-DR3. However, we make use of the stars in the sample belonging to the Trumpler-14 cluster to explore the correspondence between the sHRD and the HRD as an example.

4. Results

Tables E.1, E.2, and E.3 summarize the information about the 415 Galactic O-type stars in our initial sample. Table E.1 includes the 285 stars that we identified as likely single or SB1 for which a quantitative spectroscopic analysis was performed. The other two tables list the targets we identified as SB2 (Table E.2), or that present features in their spectra that are associated with Oe, Wolf-Rayet, and magnetic stars (Table E.3). For the latter two we did not proceed with the spectroscopic analysis, and

¹ $v(r) = v_{\infty} (1 - R_{*}/r)^{\beta}$

² $Q = \dot{M} (R v_{\infty})^{-3/2}$

³ Where we estimated the stellar radius using the calibration by Martins et al. (2005).

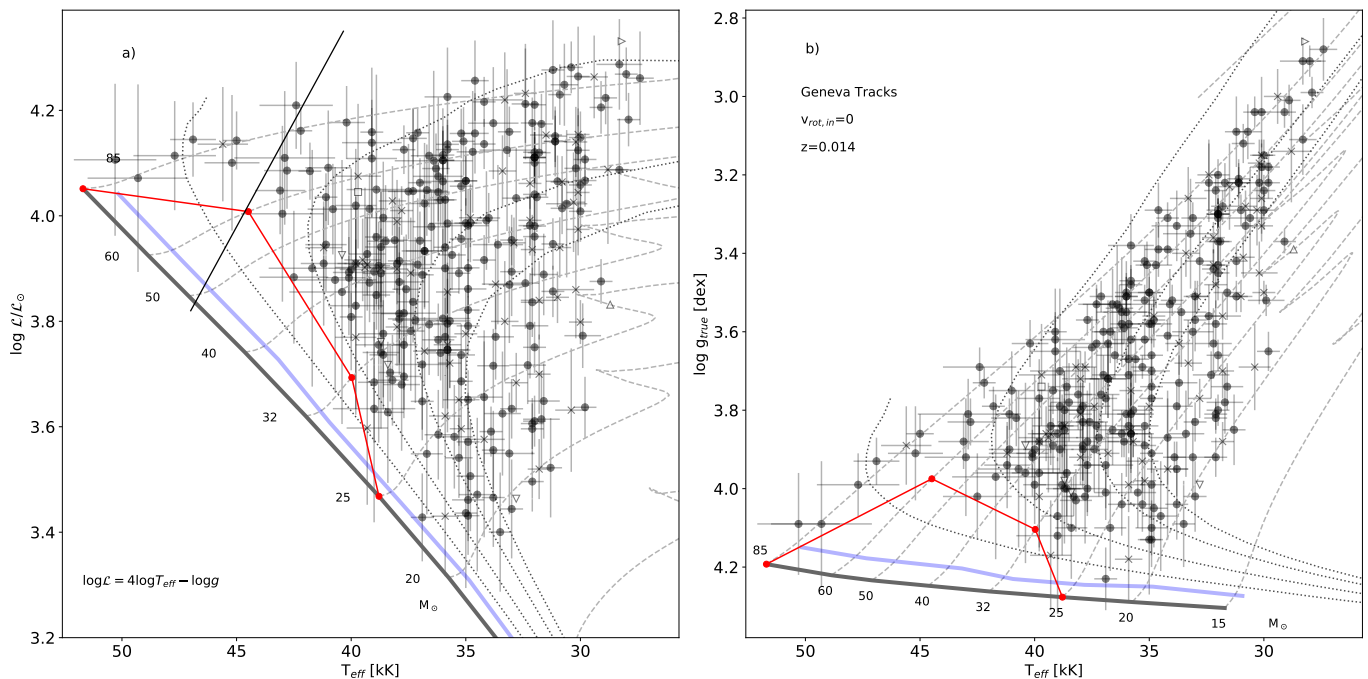


Fig. 3: Location of 285 likely single and SB1 Galactic O-type stars in the Kiel (*right*) and spectroscopic HR (*left*) diagrams. Crosses indicate stars for which we detected clear or likely signatures of spectroscopic binarity. Open symbols, triangles, and squares are stars for which only an upper or lower limit in any (triangles) or both (squares) of the two parameters used to construct these diagrams could be obtained (T_{eff} and $\log g_{\text{true}}$). Individual uncertainties are included as error bars. Evolutionary tracks and position of the ZAMS (thick solid line) from the nonrotating solar metallicity models by Ekström et al. (2012) and Georgy et al. (2013) are included for reference. The thick solid blue line represents the ZAMS for similar models, but with an initial rotation speed of 40% the critical speed. Isochrones for $\tau=1, 2, 3,$ and 4 Myr are also included. The solid diagonal black line separates the region where no He I lines are available. Last, we also delineate with a red line the region close to the ZAMS where no stars are found.

these objects are accordingly excluded from the discussion presented in Sect. 5.

In all cases, we quote the spectral classification (this also includes the classification of the secondary component of the SB2 systems whenever available) of each star (as provided in the GOSC) as well as the B -magnitude and the $E(4405\text{-}5495)$ reddening parameter (extracted from Maíz Apellániz & Barbá 2018). In addition, in Table E.1 we also include estimates and uncertainties for T_{eff} and $\log \mathcal{L}/\mathcal{L}_{\odot}$ as resulting from the IACOB-GBAT analysis (see Sect. 3). In each table, stars are grouped by luminosity class and ordered by spectral type.

The 285 stars for which we were able to obtain the spectroscopic parameters are located in the Kiel (T_{eff} versus $\log g_{\text{true}}$) and spectroscopic HR (T_{eff} versus $\log \mathcal{L}$) diagrams in Figure 3. Evolutionary tracks and isochrones from the nonrotating models at solar metallicity computed by Ekström et al. (2012) and Georgy et al. (2013) are also depicted for reference purposes. Following the discussion presented in Sect. 3, we draw in both diagrams the diagonal line indicating the boundary between the regions in which strong enough He I lines are available or are absent. While IACOB-GBAT provides a best-fitting solution for all early O-type stars to the left⁴ of this boundary line, the resulting parameters must be considered with caution (however, see the note in Sect. 3). All these stars are flagged as “weak He I lines” in Table E.1.

⁴ Several cases on the right also have specific characteristics of a helium abundance, $v \sin i$, or S/N that we consider equally limiting to the T_{eff} determination.

The most striking feature in both diagrams is the almost complete absence of stars in the mass range between ~ 30 and $70 M_{\odot}$ to the left of the 2 Myr isochrone (or below, in the Kiel diagram). There is a clear offset that increases with mass between the theoretical ZAMS and the location of the O-type stars in these diagrams. This trend disappears for stars with $\sim 85 M_{\odot}$, where stars much closer to the ZAMS are found.

As stated elsewhere (see, e.g., Repolust et al. 2004; Markova et al. 2014; Martins et al. 2015; Holgado et al. 2018), the Galactic O-type star population is mostly concentrated between the 20 and $85 M_{\odot}$ evolutionary tracks, and they are basically found to be MS stellar objects (when nonrotating Geneva models are used as reference). However, the expected good coverage of the complete MS domain is challenged by the lack of stars close to the ZAMS.

Hereinafter, the tracks and ZAMS used for comparison are always those resulting from the set of nonrotating models computed by Ekström et al. (2012). However, in Fig. 3, we also show the position of the ZAMS resulting from the Geneva models with $v_{\text{ini}} = 0.4v_{\text{crit}}$ to illustrate that the inclusion of rotation produces a small shift of the ZAMS to cooler temperatures, although this is not large enough to explain the gap between theory and observations. In a future article we will discuss why the set models including an initial rotation of 40% of the critical speed are not best suited for representing the $v \sin i$ distribution we obtain for our Galactic sample. This justifies our decision to mainly use the nonrotating models as reference here.

Our result confirms earlier findings by similar spectroscopic studies of small and intermediate-size samples of Galactic O-

type stars (*e.g.*, Herrero et al. 1992, 2007; Simón-Díaz et al. 2014; Castro et al. 2014; Holgado et al. 2018). It also mimics the results obtained by Garmany et al. (1982). This empirical result seems to also be present at other metallicities and environments, as is the case for the 30 Doradus region of the Large Magellanic Cloud (Sabiñ-Sanjulián et al. 2017).

In the next section, we present a thorough assessment of the robustness of the result presented in Fig. 3 by evaluating (1) the completeness of our magnitude-limited sample of stars, (2) potential observational biases that might affect the compiled sample, and (3) limitations and possible systematics of our analysis method. We then discuss our result in the context of various scenarios proposed so far to explain this elusive detection of O-type stars close to the theoretical ZAMS.

5. Discussion

5.1. Sample completeness and observational biases

The first question we asked ourselves before proceeding with a further interpretation of the results is whether the IACOB+OWN sample may be missing those stars that should be filling the gap. To this aim, we concentrated on the O dwarf population (luminosity class V) and evaluated the completeness of our sample with respect to the GOSC sample (see the left panel in Fig. 4).

Globally speaking, we assume that $\sim 60\%$ of the O-type dwarfs are included in GOSC. This percentage is slightly lower than that for the whole sample (see Fig. 1), but it still implies that the sample of O dwarfs surveyed by IACOB and OWN is expected to be representative enough for the purposes of our study here.

The situation further improves when we inspect the critical range of spectral types in more detail. Based on Fig. 3, and compared with Fig. 11 in Holgado et al. (2018), we determine that the missing stars probably have spectral types between $\sim O6.5$ and $\sim O4$. Because we performed several specific observing runs on which we concentrated on fainter stars than were initially considered in the IACOB and OWN projects, we could increase the number of mid-O-type dwarfs with available high-resolution spectra in these bins by roughly a factor of two, with which we reach $\sim 70-80\%$ of the GOSC sample in most cases. Although the final percentage of stars comprising the analyzed sample (and hence considered in the various sHR diagrams presented in the paper) is somewhat lower than this value (*i.e.*, $30-50\%$, see the bins in pink in the left panel of Fig. 4), this should not be considered as an indication that our sample is not complete enough for assessing the existence of the gap. This result does not imply that we miss an important fraction of the GOSC stars in these bins, but means that the remaining stars up to the mentioned $\sim 70-80\%$ have been identified as SB2 stars.

In the same line of argument, we can now try to answer the question whether based on the approximate volume defined by our sample of dwarfs and our magnitude limit, and assuming that "bare" ZAMS mid-O stars exist within this volume, we might expect to have observed them. It is straightforward to estimate absolute magnitudes⁵ for ZAMS stars; we adopted the effective temperature and luminosity at a time step of, for example, 100 000 years from the evolutionary tracks, and the bolometric corrections of Martins & Plez (2006). Assuming $(B - V)_0 = -0.28$ mag, as for typical O V stars, we find that

⁵ We recall that the absolute visual magnitude calibration of O-type stars is observational (see, *e.g.*, Walborn 1972, 1973b) and based on stars that have already evolved. It therefore follows that the absolute magnitudes of ZAMS O stars are rather fainter than these calibrations.

O V stars between 40 and 60 M_\odot very close to the ZAMS are expected to have an absolute magnitude $M_B = -5.2, -5.7$. Considering a fairly simple average extinction law as a function of galactic position (Amores & Lepine 2004), this would imply that, for example, with a limiting magnitude of $M_B \sim 8$, we should observe such stars within 2–2.5 kpc, depending on galactic longitude (and assuming low galactic latitude). More specifically, at the distance to Trumpler-14 (parallax of 0.42 mas, see Appendix B and Sect 5.3.2), these stars would have apparent magnitudes of $B \sim 7.9, 7.5$. Even considering a greater extinction, which would produce a reduction of up to two apparent magnitudes, these stars would be marginally included among the stars observed at high resolution, and they would definitely be included in the GOSC sample.

One last question we wish to investigate in this section is whether our sample of stars is affected by the possible observational bias associated with the extinction effect produced by dense material that may be still surrounding the star while the star evolves from the ZAMS. This material is expected to block mostly shorter wavelengths, producing a general reddening trend (Yorke 1986; Castro et al. 2014). Therefore, if we are missing O-type dwarfs in GOSC with a high value of the reddening parameter, this may imply that the empty region might be filled by them.

To evaluate this possibility, we present in Fig. 4 two histograms of stars versus the reddening parameter $E(4405-5495)$, as obtained by Maíz Apellániz & Barbá (2018). We separated the sample into two parts, considering stars with spectral types earlier and later than O6.5, respectively. Although in the sample of late O-type stars we lack the great majority of stars with $E(4405-5495) > 1.0$, the expected location of these stars in the spectroscopic HR diagram is below the problematic region (in the sHRD, see Fig. 3), and we therefore do not discuss them further.

For the sample of mid- and early O-type stars, on the one hand, we highlight that of the 19 stars in GOSC with intermediate values of the reddening parameter ($E(4405-5495) \sim 1.0 - 1.5$), we obtained spectroscopic parameters for 6 of these stars and detected 3 stars as SB2. All of the missing 10 stars are located at a distance (following Bailer-Jones et al. 2018) larger than 2.5 kpc that reaches up to 7–8 kpc in some cases. The extinction values of all the missing stars therefore likely come from their large distance. On the other hand, none of the seven stars with high values of the reddening parameter ($E(4405-5495) \sim 1.5 - 2.0$) are included in the list of 285 stars for which we have spectroscopic parameters. In addition, distance estimates for these stars are in the range 1.5–3 kpc; this is not extremely far away. Although this is a small sample, it would be very interesting to obtain spectra and parameters for these stars in the future, with the aim of identifying whether these stars are found closer to the ZAMS than the other stars in our sample. In addition, this study might help to identify potential correlations between high extinction and extreme youth, such that these stars may represent a newborn generation, or at least a less evolved population. In this regard, further exploration of the information available about the local environment (to identify whether these stars are located in dusty and young H II regions, see also the notes in Sect. 5.3.1) could be informative.

We therefore conclude with relatively good confidence that the existence of a gap is apparently neither due to the fact that our sample of O dwarf stars is small nor to a lack of those stars that should be filling the empty region (at least for likely single and SB1 stars). An in-depth analysis of the stars with very high extinction will shed additional light on the matter.

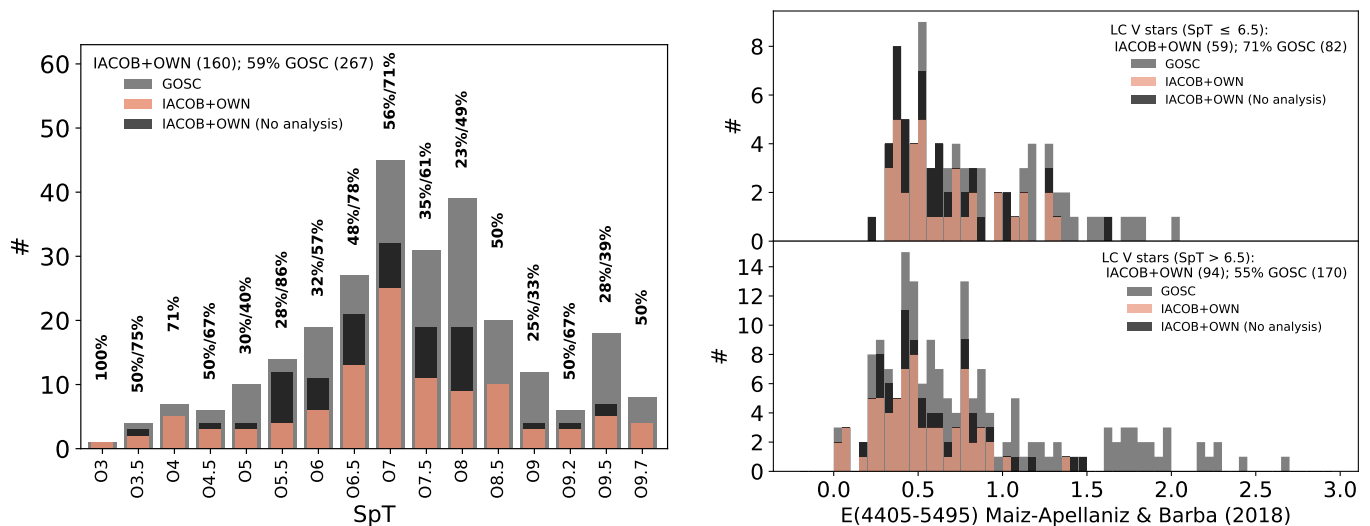


Fig. 4: Comparison of our working sample of Galactic O dwarfs (pink and black) with respect to those included in GOSC (gray). *Left* Same as Fig. 1, but only for luminosity class V stars. *Right* Histograms of the reddening parameter ($E(4405-5495) \sim E(B-V)$) separated by ranges in spectral type: earlier (top) and later (bottom) than O6.5.

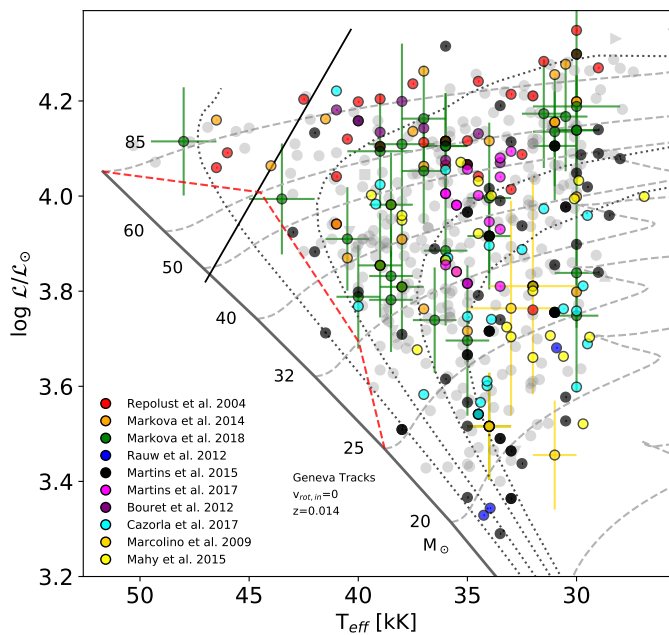


Fig. 5: Same as Fig. 3, but overlotted on our results those obtained by previous spectroscopic studies of small and medium-size samples of Galactic O-type stars found in the literature. Uncertainties are not plotted for cases in which a single value is considered as a standardized error in that particular study.

5.2. Limitations of the method

In this section we investigate the possibility that the lack of stars close to the ZAMS in the sHR and Kiel diagrams (Fig. 3) is produced by some problem in our method. In particular, we evaluate whether our IACOB-GBAT analysis might erroneously provide gravity estimates below the actual value. This situation may help to fill the gap.

In the past decade, several spectroscopic studies have investigated small and medium-size samples of Galactic O-type

stars by means of the modern generation of stellar atmosphere codes and different (but related) analysis strategies. While most of these studies were based on the analysis of the optical spectrum (*e.g.*, Repolust et al. 2004; Markova et al. 2014, 2018; Martins et al. 2015, 2017; Cazorla et al. 2017), some of them performed a combined optical+UV analysis (Marcolino et al. 2009; Bouret et al. 2012; Mahy et al. 2015). Figure 5 includes the results of all these studies overlotted on our distribution of stars in the sHR diagram. We remark that practically all the stars in the combined sample compiled from the literature are also included in our sample; in addition, we find that our work has allowed us to increase the number of Galactic O-type stars with available spectroscopic parameters by almost a factor 3 (or 5 when we consider the complete IACOB+OWN sample).

Despite the diversity in methods and the use of different stellar atmosphere codes, only one star in the compiled sample is located in the gap region. (However, we note that this star is also included in our analyzed sample and our result differs from the result obtained by Martins et al. (2015), see Appendix A.) This result, together with the relatively good agreement found in Holgado et al. (2018) between the effective temperatures and surface gravities obtained with the FASTWIND and CMFGEN codes for a sample of ~ 100 stars, allows us to stress that the lack of detected O-type stars with ages $\lesssim 1.5$ Myr and intermediate masses ($\sim 30-60 M_{\odot}$) is a general outcome of all spectroscopic studies performed to date found in the literature, and it is not necessarily associated with limitations or systematics present in our analysis strategy. Interestingly, our much larger sample has allowed us to better define the gap region by finding a non-negligible number of late O-type stars closer to the ZAMS than were previously found. The results support our argument even more that the gap is not a result of observational biases associated with a magnitude-limited sample because these late O-type stars are $\sim 0.5-1.5$ mag fainter than those that would be occupying the gap region.

We can also wonder whether the solution to this peculiar empirical feature is associated with any missing ingredient in current stellar atmosphere codes. In this line of argument, in a recent study by Markova et al. (2018), where the authors reassessed the

long-standing mass discrepancy problem (Herrero et al. 1992), it was claimed that part of the reason might be linked to a systematic underestimation of the surface gravities resulting from not accounting from the microturbulent pressure term in the hydrodynamic and quasi-hydrostatic equations when the stellar atmosphere structure was computed. As indicated in Markova et al. (2018), and to serve as an illustrative example, for a star with $T_{\text{eff}} = 40$ kK, a microturbulence of $15 - 20 \text{ km s}^{-1}$ would increase the value of $\log g$ by $\sim 0.1 - 0.15$ dex if it were accounted for as a pressure term.

While this is an interesting hypothesis to be further investigated, it also implies some caveats for the case of the mass discrepancy problem (see notes in Markova et al. 2018) and for this paper. For example, if we were to relocate the entire distribution of O-type stars shown in the right panel of Fig. 3, some of the late and early O-type stars would be placed below the ZAMS (if the same correction factor were assumed, which may not necessarily be the case). In addition, while this solution may solve both the mass discrepancy problem and the lack of stars close to the ZAMS, it is interesting to note that Markova et al. (2018) found that the mass discrepancy problem is less pronounced precisely in the mass range where the void of O-type stars near the ZAMS appears (between the 32 and $50 M_{\odot}$ evolutionary tracks).

5.3. More empirical insights

5.3.1. Morphological signatures of youth: O Vz stars

The O Vz phenomenon is a spectroscopic peculiarity defined by a stronger He II 4686 absorption than in other He lines compared to that found in typical class V spectra (Walborn & Parker 1992; Walborn 2009). This spectroscopic feature was originally proposed to be a clear indication of youth and hence proximity to the ZAMS (Walborn & Blades 1997). However, as thoroughly discussed in Sabín-Sanjulián et al. (2014), the situation is more complex, and specific combinations of T_{eff} , $\log g$, $\log Q$, and $v \sin i$ might cause the spectrum of an O dwarf to present the Vz characteristic, in principle independently of age or proximity to the ZAMS. They also note that the Vz characteristic disappears for T_{eff} below $35\,000$ K.

We here followed the quantitative methods defined in Arias et al. (2016) to identify the O Vz stars in our sample. We note that the study by Arias et al. (2016) takes into account the results by Sabín-Sanjulián et al. (2014) and provides evidence that these stars are associated with dusty and young H II regions, for which an independent value of age might be constrained from its morphology.

Figure 6 shows the distribution of the O Vz stars in our sample in the sHRD. These stars, highlighted at the top of the complete sample, clearly delineate the young boundary of the distribution of stars (*i.e.*, they are the stars closest to the ZAMS); however, they are still an equivalent of ~ 0.2 dex away in surface gravity (if we compare them with lines of constant $\log g$, see Fig. 2) from the theoretical ZAMS defined by the Ekström et al. (2012) models.

This result once more emphasizes our statement that our sample does not miss O-type stars (detectable in optical wavelengths) that should be closer to the ZAMS due their plausible youth.

5.3.2. An extremely young cluster: Trumpler-14

One possible inference from Fig. 3 is that our data set does not contain clusters that are young and massive enough to populate

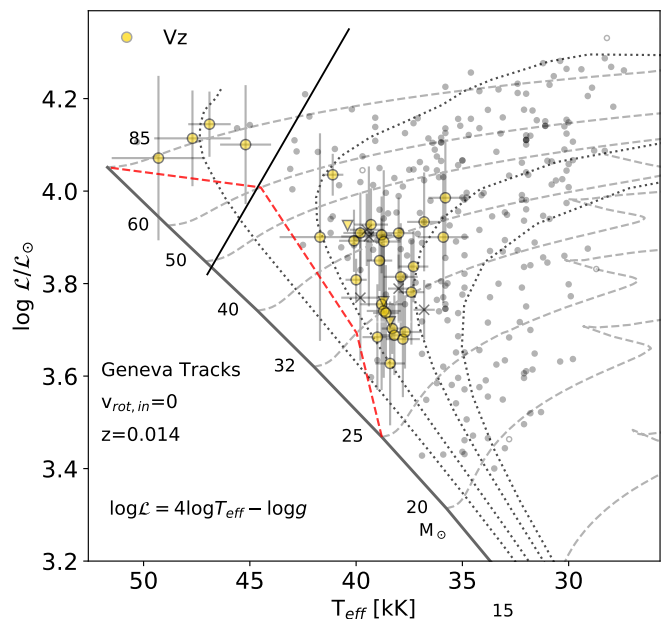


Fig. 6: Same as Fig. 3 but highlighting the Vz stars in our sample.

the gap. For example, except for the most massive stars in the sample, an isochrone with an apparent age of ~ 2 Myr is a reasonable fit to the lower envelope of the O stars, particularly around mid-O spectral types. Interestingly, most of the very massive stars that are close to the ZAMS lie within the Carina region, which is one of the youngest and most massive star-forming regions in the Galaxy.

Carina is a complex region that hosts a number of clusters. Two in particular, Trumpler-14 and Trumpler-16, are thought to be very young, with ages in the range $1 - 3$ Myr (Walborn 1973a; Massey & Johnson 1993; Smith 2006; Hur et al. 2012; Damiani et al. 2017). As discussed in the literature, Trumpler-14 in particular is generally determined to be the younger of the two, based largely on the presence of more-evolved massive stars in Trumpler-16. Sana et al. (2010) have estimated an age of 0.4 Myr from the study of its pre-MS stars, thereby providing us with an age that is independent of the MS evolutionary tracks we wish to test. Clearly, the stars in our sample that belong to this extremely young cluster provide powerful diagnostic insight into the gap between models and observations.

However, because the two clusters lie very closely together on the sky, the cluster members might be confused, see, for example, the discussion in Walborn (1973a) and Smith (2006), and care must therefore be taken to identify bona fide members of these two clusters. In Appendix B we therefore discuss the Trumpler-14 and Trumpler-16 cluster membership for stars in GOSC, based on *Gaia*-DR2 (Gaia Collaboration et al. 2018a; Lindegren et al. 2018) spatial and dynamical characteristics. We find 17 stars in Trumpler-14 and 20 stars in Trumpler-16 (whereas GOSC lists 14 and 24 members, respectively).

Ultimately, we decided to work solely with the Trumpler-14 sample (see Table 1), because (a) we had more stars with spectroscopic analysis results (eight versus seven for Trumpler-16), (b) they included most of the very massive stars located in the seemingly separated group in the upper left part of the sHRD, and (c) Trumpler-14 is extremely young. We note that this list is not intended to be complete, rather it is intended to represent

Table 1: O-type stars in Trumpler-14. For ten stars, high-resolution spectra are available (two of them are SB2 stars), and seven stars are only listed in GOSC. Columns detail name, spectral class following GOSSS, B -magnitude, reddening parameter $E(4405-5495)$, T_{eff} , parameter \mathcal{L} , and luminosity, variability notes from this work, and from MONOS (Maíz Apellániz et al. 2019). T_{eff} and luminosity errors from G_{BAT} χ^2 distributions (See Holgado et al. 2018), and limited to 500 K (half of the step in the grid). \mathcal{L} uncertainty from T_{eff} and $\log g_{\text{true}}$ error propagation.

Name	SpT LC	B [mag]	$E(4405-5495)$ [mag]	T_{eff} [kK]	$\log \mathcal{L}/\mathcal{L}_{\odot}$ [dex]	$\log L$ [dex]	Notes this work	Notes MONOS
high-resolution spectra available								
HD 93129 AaAb ^a	O2 If*	7.8	0.514	45.6±1.1	4.14±0.11	6.38±0.03	SB1	SB2/3
HD 93129 B ^a	O3.5 V((f)z)	9.0	""	47.7±1.8	4.11±0.10	6.43±0.05	C	C
HD 93128	O3.5 V((fc)z)	9.2	0.529	49.3±2.2	4.07±0.18	5.78±0.06	C	C
HDE 303311	O6 V((f)z)	9.1	0.414	40.1±0.7	3.89±0.07	5.16±0.02	C	C
CPD -58 2611	O6 V((f)z)	9.9	0.562	39.8±0.8	3.91±0.09	5.24±0.02	C	SB1?
HD 93161 B ^b	O6.5 IV((f))	8.7	0.530	37.1±0.8	3.91±0.13	5.74±0.03	C	SB1/2?
HD 93160 AB	O7 III((f))	8.2	0.416	36.6±0.7	3.79±0.10	5.68±0.02	LPV	SB1?
HD 93161 A ^b	O7.5 V	8.6	""	.	.	.	SB2	SB2
Trumpler 14-9	O8.5 V	10.1	0.455	36.7±0.7	3.55±0.11	5.05±0.02	C	VAR
HD 93249 A	O9 III	8.5	0.382	.	.	.	SB2	SB2
high-resolution spectra not available in IACOB-OWN								
CPD -58 2620	O7 V((f)z)	9.4	0.407	C
ALS 15204	O7.5 Vz	11.5	0.787	SB2
Tyc 8626-02506-1	O9 V(n)	11.5	0.591
ALS 15207	O9 V	11.1	0.635
CPD -58 2625	O9.2 V	11.1	0.661	VAR? SB2?
CPD -58 2627	O9.5 V(n)	10.4	0.483
HDE 303312	O9.7 IV	10.3	0.547	Probable SB2

^a & ^b Only one entry for $E(4405-5495)$ in Maíz Apellániz & Barbá (2018)

C: Constant, LPV: Line profile variability, VAR: variability

stars that based on their spatial and dynamical properties, are high-probability members of Trumpler-14.

In Fig. 7 we present the sHRD distribution of Trumpler-14 stars with spectroscopic results with respect to the rest of the sample. For comparison, the tracks provided by the Geneva models (Ekström et al. 2012) are included. Again, we see the same result as with the complete sample. There are no stars near the ZAMS between the tracks of 32 to 60 M_{\odot} . The presence of the moderately large group of very high-mass stars (3 stars with $\sim 85 M_{\odot}$) so close to the ZAMS indicates a very young age, in agreement with Sana & Evans (2011), but it is noticeable that there are no intermediate-mass stars close to the ZAMS.

Figure 8 shows an area of $\sim 10'$ around the center of the Trumpler-14 cluster and depicts GOSC stars that we have considered to belong to Trumpler-14 for which we have IACOB results as well as those for which we do not have high-resolution spectra or spectroscopic results. We have stellar parameters for half of the stars (8 out of 17) that also represent the most cohesive group, with a number in the center of the cluster. For the other 9 stars without parameters, we have a spectral type classification from GOSSS, showing us that only two stars have spectral types O7-7.5 and the rest have spectral types later than O9. These stars are not expected to be able to fill the gap region. Therefore our sample is not biased with respect to GOSC in terms of spectral type, and is representative for the cluster's youth.

As discussed in section 3, our reason for using the sHRD instead of the classical HR is the lack of reliable distance measurements for all the stars analyzed in the sample to derive luminosities. The idea of the sHR diagram (presented in Langer & Kudritzki 2014) is to replace the luminosity (L) with the quantity $\mathcal{L} = T_{\text{eff}}^4/g_{\text{true}}$, which is the inverse of the flux-weighted gravity introduced by Kudritzki et al. (2003). It depends only on vari-

ables that can be directly derived from stellar spectra without knowledge of the stellar distance or the extinction, and it presents horizontal stellar evolutionary tracks for massive stars. The differences and possible caveats between these two diagrams are discussed in Langer & Kudritzki (2014) or Castro et al. (2014), but for this particular topic of stars near the ZAMS, the results are analogous, as can be seen in studies using the HR diagram with similar results (Sabín-Sanjulián et al. 2017; Schneider et al. 2018). It is possible, however, that if gravity measures are systematically inaccurate, the gap would only appear for the sHRD, but these cases should be studied individually, and a rather large systematic error (~ 0.25 dex) would be necessary to reconcile models and observations.

Here, we evaluate the possibility that the discrepancy only appears in the sHRD and disappears when we build the classic HR diagram. An extensive discussion of sHRD versus HRD can be found in Markova et al. (2018). It is necessary then to obtain a distance measurement, and to derive the luminosity for each star. In this case, we decided to estimate a single distance to the group of stars that make up one cluster, Trumpler-14. The strength of this method is that the combination of the parallax values for all the available stars of a cluster eliminates the possible dispersion or even some systematic problems. For example, *Gaia* parallaxes present problems for bright stars, which many O stars are (Luri et al. 2018). On the other hand, it is important to confirm that the analyzed stars really belong to this cluster, so that the combination of values is valid. For Trumpler-14, around 100 stars with *Gaia* data were used to determine a parallax of 0.42 mas (see Appendix B and Luri et al. 2018), based on a method analogous to the work of Davies & Beasar (2019), including the correction for the systematic offset of -0.03 mas (Gaia Collaboration et al. 2018b). Using this value, we calculated absolute magnitudes and

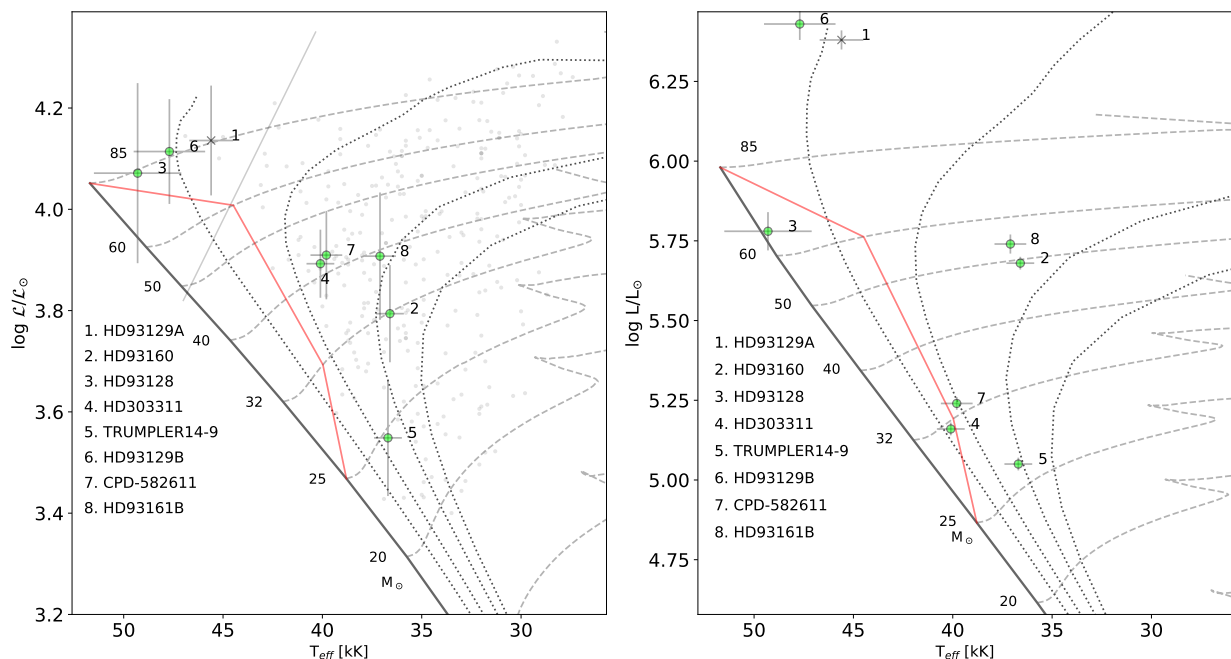


Fig. 7: Location (and identifier) of the eight Trumpler-14 stars with available spectroscopic parameters in our sample in the sHR (*left*) and original HR (*right*) diagrams. The sHR diagram includes the remaining sample for comparison. Crosses indicate stars for which we have detected clear or likely signatures of spectroscopic binarity. Individual uncertainties are included as error bars. Evolutionary tracks and the position on the ZAMS from the nonrotating solar metallicity models by Ekström et al. (2012) and Georgy et al. (2013) are included for reference. Isochrones for $\tau=1, 2, 3,$ and 4 Myr are also included. A solid light gray line is drawn to separate the region where no He I lines are available. Using selected points of the evolutionary tracks in the sHRD to delineate the gap of stars near the ZAMS (see Appendix D), we are able to transport an analogous region to the HR diagram (red line).

then luminosities of the O stars of our sample belonging to the cluster, following standard procedures (Kudritzki 1980; Herrero et al. 1992; Repolust et al. 2004). Then we combined the radius with the temperature to obtain the luminosity. Fig. 7 shows the 8 stars in Trumpler-14 for which we have results in the HR diagram. The error bars shown are the formal error of our analysis, which greatly underestimate the actual error. A more realistic error, based on the distance uncertainty, would be around $\log L \pm 0.05$ [dex].

Analyzing the result more in depth, we note that the position (on the Y-axis) of half the stars has varied. Very hot stars have moved very high or low from their original position in the sHRD, but they still play their role as very young stars in the sample. HD 93128 is now well within the gap area; however, we recall that the parameters obtained for stars with such a high T_{eff} are not properly constrained with our method (due to the lack of He I lines). This result indicates that the shape of the gap region must be taken with care when the region above the $60M_{\odot}$ evolutionary track is considered because their limits are still not precisely defined. Two stars of intermediate spectral type (O6) have moved below their original position, approaching the ZAMS and moving from the 2-3 Myr interval to the 1-2 Myr range. At the same time, their apparent youth has increased, they have moved to the part of the diagram where there was less discrepancy between models and observations. They have not entered the gap region. At first glance, it might be concluded that the problem has not been corrected when the HR diagram that includes the O-type stars in Trumpler-14 is inspected; however, a closer inspection of Fig. 7 indicates that this is not the best sample to extract any firm conclusion in these regards. All considered stars

have effective temperatures higher than ~ 45000 K or lower than ~ 38000 K, which means that the intermediate range in T_{eff} where the gap region is mainly located is missing. Because switching from the sHRD to the HRD only affects the Y-axis, Trumpler-14 cannot be used to evaluate the possible effect on using the HRD instead of the sHRD when the presence of mid O-type stars close to the ZAMS is investigated.

5.3.3. Role of a stochastic IMF in Trumpler-14 and the whole sample

The particular case of studying an isolated cluster could be biased due to the stochastic nature of the initial mass function (IMF) in the formation of massive stars, or even due to the ill fortune of not having observed a pair of stars belonging to the cluster that could cover the void region. This bias disappears when the original complete sample of O stars is considered, but we decided to conduct the particular study in Trumpler-14 because it is one of the youngest clusters to which our survey has access.

In a first step, we evaluated the completeness of our sample of massive Trumpler-14 stars. We assumed a mass of Trumpler-14 close to $4 \cdot 10^5 M_{\odot}$ (Sana et al. 2010; Hur et al. 2012; Alexander et al. 2016) and a Kroupa IMF (Kroupa 2001). The mean mass per star of this IMF is $0.357 M_{\odot}$ (with a mass limit between $120-0.01 M_{\odot}$), which translates into $N_{*} \sim 11203$ stars in the cluster for the given cluster mass. This IMF also provides a probability that the mass of a random star is in the $25 - 60 M_{\odot}$ mass range of $p_{[25,60]} = 5.14 \cdot 10^{-4}$, and $p_{[60,120]} = 1.38 \cdot 10^{-4}$ for the $60 - 120 M_{\odot}$ mass range. When we use the 11 203 stars

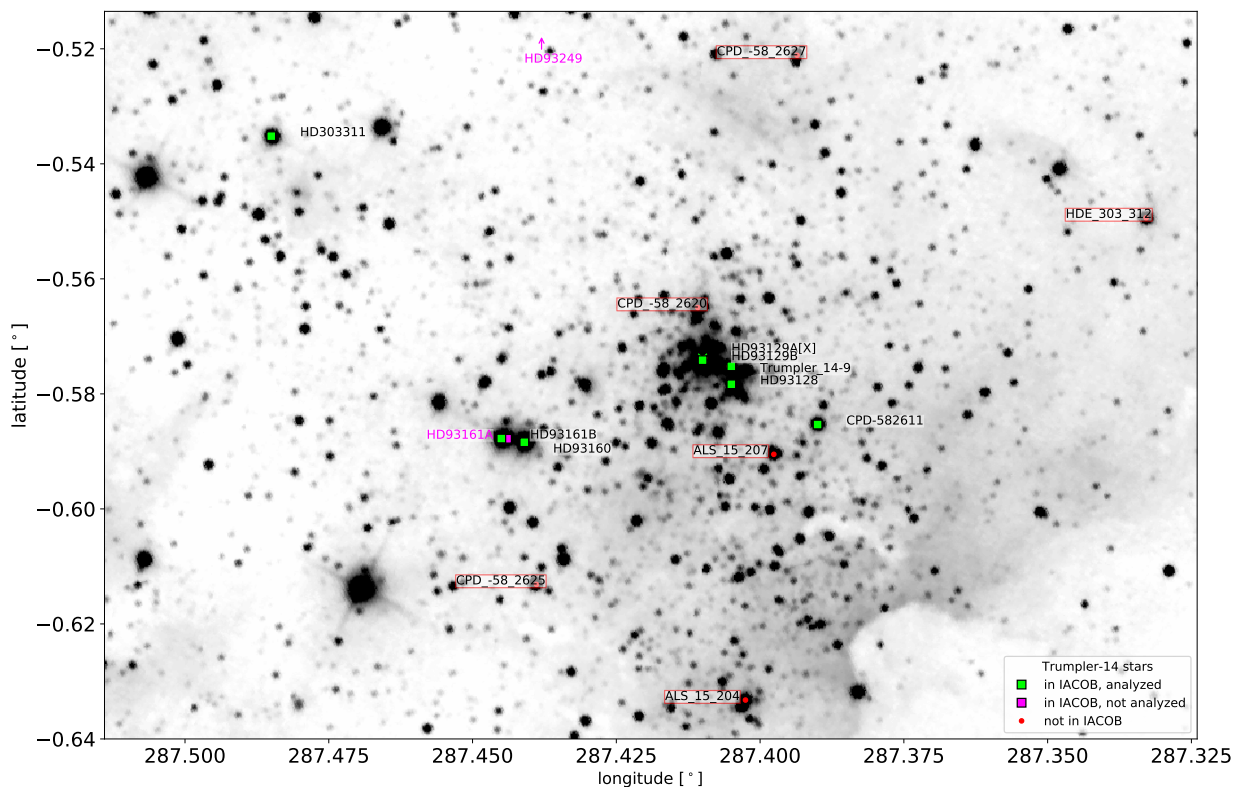


Fig. 8: Inverse 2MASS J-filter image showing a 10' FoV of Trumpler-14, with the position and name of O-type stars in the sample assigned to the cluster (see Sects. 5.3.1 and 5.3.2 for further details). Different colors represent different status: green represents stars with spectroscopic parameters, magenta are SB2 stars for which no quantitative analysis is possible, and red marks stars without high-resolution spectra.

and the previous probabilities in a multinomial distribution, the expected number of stars in the $25 - 120 M_{\odot}$ mass range is 7 ± 4 at a 90% confidence interval, which is consistent with our census of 10 stars in this mass range. More in detail, the probability of finding exactly 7 stars is 14.8%, the probability of finding exactly 10 stars is 8%, and finally, the probability that the cluster would have more than 12 stars in this mass range is 3.6%. Accordingly, the probability of finding exactly 13 stars is 1.8%. In summary, for the assumed mass and IMF, we are therefore relatively confident that our star census is complete.

In a second step, we investigated how likely a configuration would be for which no star is found in the $25 - 60 M_{\odot}$ mass range and three stars appear in the $60 - 120$ mass range. This would correspond to a two-bursts scenario where all the lower mass stars were formed more than 2 Myr ago, and the three more massive stars observed were formed in the last 2 Myr. We assumed that each of these two bursts formed half of the stars each (± 1 because N_* is an even number). In this case, the probability⁶ of having zero stars in the $60 - 120 M_{\odot}$ mass range given that there are seven stars in the $25 - 60 M_{\odot}$ mass range is 46%. On the other

hand, the probability of having zero stars in the $25 - 60 M_{\odot}$ mass range given that there are three stars in the $60 - 120 M_{\odot}$ mass range is 5.7%. With this value, although it is low, we cannot discard the possibility that the gap observed in Trumpler-14 is due to IMF sampling effects. It is highly improbable, but plausible. However, we note that these oddities increase when the number of stars considered increases. As an example, the probability of having zero stars in the $25 - 60 M_{\odot}$ mass range given 3 stars in the $60 - 120 M_{\odot}$ mass range and $N_* = 11203$ drops to 0.3%. This situation would correspond to the case where Trumpler-14 and Trumpler-16 are considered as a whole (this would require a study of Trumpler-16, which is beyond of the scope of this paper). Finally, the situation would become even more improbable when the overall IACOB sample is taken into account, but again, a study like this would require evaluating the different star formation history of all the clusters included in the sample.

5.4. Some insights from stellar evolution modeling

5.4.1. ZAMS and theoretical birthline of massive stars

We described in Sect. 1 that the formation path of a star is defined as the birthline, which in massive stars (with standard accretion rates) could pass through stellar fusion ignition (ZAMS) before reaching complete accretion of its birth cloud. For a fixed accretion rate, all massive stars follow the same birthline until accretion stops, reaching their maximum masses and continuing then through a canonical evolutionary track. The position in the HR (or sHR) diagram of a star largely depends on the amount of hydrogen that has already been consumed in its core through

⁶ This probability can be obtained directly by the Bayes theorem over the associated multinomial distribution. For the particular case of the probability of $n_{[25-60]} = 0$ given that $n_{[60-120]} = n_a$ is

$$P(n_{[25-60]} = 0 | n_{[60-120]} = n_a; N_*) = \left(\frac{1 - P_{[25-60]} - P_{[60-120]}}{1 - P_{[25-60]}} \right)^{N_* - n_a}. \quad (1)$$

Similarly for other cases as $P(n_{[60-120]} = 0 | n_{[25-60]} = n_a; N_*)$ when the corresponding changes have been made.

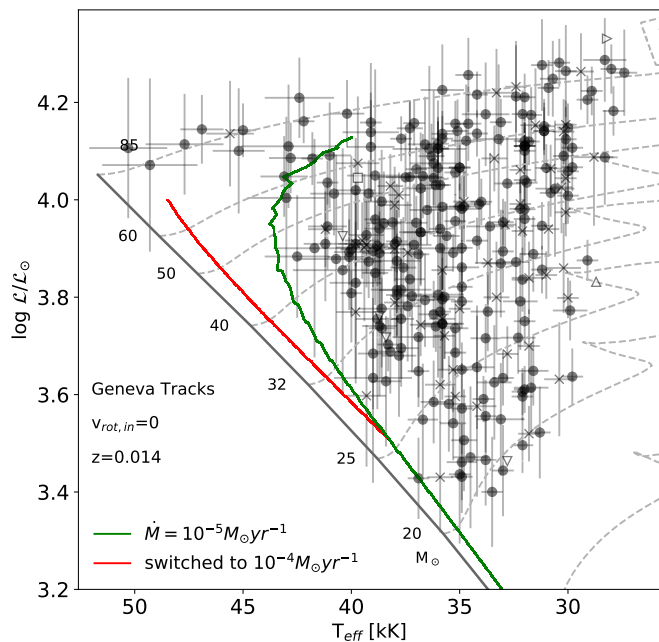


Fig. 9: Same as Fig. 3. Additional evolutionary tracks of the model evolving at mass accretion $\dot{M} = 10^{-5} M_{\odot} \text{yr}^{-1}$ (solid green). The red track corresponds to the model in which the evolution is switched from $\dot{M} = 10^{-5} M_{\odot} \text{yr}^{-1}$ to $10^{-4} M_{\odot} \text{yr}^{-1}$ at $M = 25 M_{\odot}$.

fusion processes. For a slower accretion rate, the evolution of the star is also slower and allows enough time for hydrogen to be consumed. This would cause the star to move in the HR (or sHR) diagram in an upward right direction (see e.g., Vanbeveren et al. 1998). We determined whether it is possible to reconcile the two models (the birthline) and observations by adjusting or tuning their critical factor, the accretion history included in the models. The process for generating the models with different accretion parameters and their evolutionary tracks is described in Appendix C. Here we only discuss the shape of the tracks in the region of the HR diagram that corresponds to the observations. The tracks are shown on Figs. 9, 10, and 11.

When the gap near the ZAMS in the OB range is to be interpreted as an effect of accretion, the accretion track has to correspond to the left-hand side envelope of the observations, that is, the birthline⁷. When a star on the accretion track reaches its final mass, its subsequent evolutionary track is toward the red, where observations show the presence of stars. This is in our case, when the accretion time is longer than the KH time.

Fig. 9 shows that the model simulations accreting at $\dot{M} = 10^{-5} M_{\odot} \text{yr}^{-1}$ match the envelope of the observations well, except for the series of very high-mass stars. As explained throughout this article, stars in this region are susceptible to large uncertainty due to the absence of He I diagnostic lines. This model simulation reaches the ZAMS at a relatively low mass ($M \approx 8 M_{\odot}$, not visible in the plot). After this, as accretion proceeds, the model approximately follows the ZAMS toward the blue until $M \approx 30 M_{\odot}$. Then it shifts toward higher luminosi-

⁷ Observationally, the birthline is sometimes defined as the line on the HR diagram (or sHRD) along which young stars become visible in the optical (Fig. 1 in Haemmerlé et al. 2019). The birthline of massive stars is expected to correspond to the lower envelope of the observations (Haemmerlé et al. 2019).

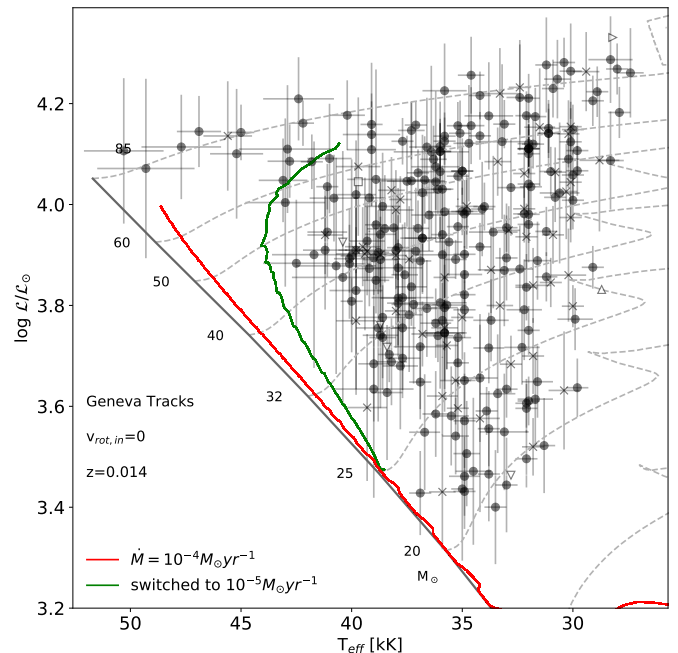


Fig. 10: Same as Fig. 9 for $\dot{M} = 10^{-4} M_{\odot} \text{yr}^{-1}$ (solid red). The green track corresponds to the model in which the evolution is switched from $\dot{M} = 10^{-4} M_{\odot} \text{yr}^{-1}$ to $10^{-5} M_{\odot} \text{yr}^{-1}$ at $M = 25 M_{\odot}$.

ties, and at $M \approx 50 M_{\odot}$, it starts to move significantly toward the red as a result of the MS evolution. This can be understood by comparing the timescales for accretion ($t_{\text{accret}} = M/\dot{M}$) and MS evolution (t_{MS}). For instance, at $M = 10 M_{\odot}$, the former is $t_{\text{accret}} = 1 \text{ Myr}$, more than one order of magnitude shorter than the latter ($t_{\text{MS}} \approx 20 \text{ Myr}$, Schaller et al. 1992). In this mass range, the star can therefore efficiently grow in mass before it evolves significantly on the MS. As a consequence, its track remains close to the ZAMS as accretion proceeds. For $M = 30 M_{\odot}$, the two timescales become comparable ($t_{\text{accret}} = 3 \text{ Myr}$ and $t_{\text{MS}} \approx 6 \text{ Myr}$). The effects of accretion and MS evolution both affect the evolutionary birthline track, which is progressively shifted from the ZAMS. Finally, at $M = 50 M_{\odot}$, the accretion time becomes longer than the MS time ($t_{\text{accret}} = 5 \text{ Myr}$ and $t_{\text{MS}} \approx 4 \text{ Myr}$), the effect of MS evolution on the track dominates that of accretion, and the star moves away from the ZAMS.

The models at $10^{-4} M_{\odot} \text{yr}^{-1}$ (Fig. 10) and $10^{-3} M_{\odot} \text{yr}^{-1}$ (Fig. 11) show a different behavior. These two models reach the ZAMS at higher masses, $M \approx 15 M_{\odot}$ and $40 M_{\odot}$, respectively. At these rates, the accretion time always remains shorter than 1 Myr until the final mass of the runs ($t_{\text{accret}} < 70 M_{\odot}/10^{-4} M_{\odot} \text{yr}^{-1} = 0.7 \text{ Myr}$), while the MS time always remains longer than 3 Myr. Thus the evolutionary tracks are determined essentially by accretion, and almost follow the ZAMS as accretion proceeds.

The relevant accretion rate for estimating the accretion time is the current rate. As a consequence, the models with an accretion rate that changes at $M = 25 M_{\odot}$ do not keep memory of their past accretion history. The tracks of these models are shown in Figs. 9, 10, and 11. A star with $M > 25 M_{\odot}$ that accretes at $\dot{M} \geq 10^{-4} M_{\odot} \text{yr}^{-1}$ follows the ZAMS as accretion proceeds, independently of the previous accretion history (red track in Fig. 9). In contrast, a star with $M > 25 M_{\odot}$ accreting at $\dot{M} = 10^{-5} M_{\odot} \text{yr}^{-1}$ always evolves away from the ZAMS, even

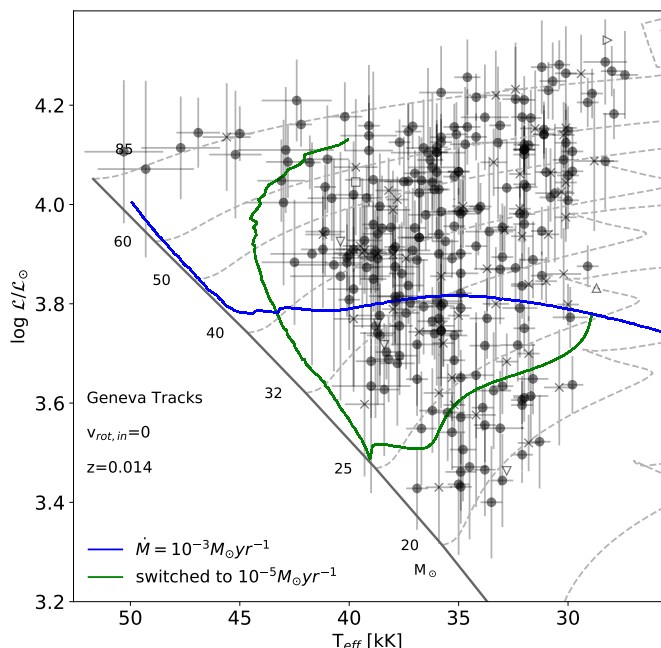


Fig. 11: Same as Figs. 9 and 10 for $\dot{M} = 10^{-3} M_{\odot} \text{yr}^{-1}$ (solid blue). The green track, which begins at the blue line at $M = 25 M_{\odot}$, corresponds to the model in which the evolution is switched from $\dot{M} = 10^{-4} M_{\odot} \text{yr}^{-1}$ to $10^{-5} M_{\odot} \text{yr}^{-1}$ at $M = 25 M_{\odot}$.

if it accreted at $\dot{M} \geq 10^{-4} M_{\odot} \text{yr}^{-1}$ for $M < 25 M_{\odot}$ (green tracks in Figs. 10 and 11).

5.4.2. Constraints on accretion history from observations

In accordance with previous suspicions from Vanbeveren et al. (1998), the models described in the previous section show that for the birthline to fit the envelope of the observations, the accretion rate must not exceed $10^{-5} M_{\odot} \text{yr}^{-1}$ in the mass range $M \gtrsim 25 M_{\odot}$. This result is counterintuitive because for massive stars, typical accretion rates of $10^{-3} M_{\odot} \text{yr}^{-1}$ are expected (Larson & Starrfield 1971; Hosokawa & Omukai 2009; Kuiper et al. 2010a).

This suggests that a typical accretion history given by

$$\dot{M} = \begin{cases} 10^{-3} - 10^{-5} M_{\odot} \text{yr}^{-1} & \text{for } M \lesssim 25 M_{\odot} \\ 10^{-5} M_{\odot} \text{yr}^{-1} & \text{for } M \gtrsim 25 M_{\odot} \end{cases} \quad (2)$$

The accretion history of massive stars remains an open question. Hydrodynamical simulations of the pre-stellar collapse show a rich variety of behaviors, with rates that increase or decrease with time, depending essentially on the initial conditions (e.g., Peters et al. 2010a,b,c, 2011; Kuiper et al. 2010b, 2011; Girichidis et al. 2011, 2012a,b; Meyer et al. 2018). Observations of outflows around massive young stellar objects (or MYSOs) and of the distribution of Herbig Ae/Be stars on the HR diagram suggest a rate that increases with the stellar mass (Behrend & Maeder 2001; Haemmerlé et al. 2019). This behavior is supported by the luminosity distribution of massive protostars in the Milky Way (Davies et al. 2011). On the other hand, the probability dependence of the rate on the stellar mass does not necessarily reflect an evolutionary sequence. More massive objects might form at higher rates during the main accretion phase, before the rate declines. Many reasons might explain the decrease

in the accretion rate as a function of the mass of the accretor, such as the effect of the rising UV feedback (Peters et al. 2010c) as the stellar surface heats up, the increase of radiation pressure (Kuiper et al. 2010b), or the angular momentum barrier (Haemmerlé et al. 2017).

5.4.3. Very massive stars in the sample

Our sample of 285 O-type stars with spectroscopic parameters includes a small group of 6 early O-type stars with evolutionary masses $\sim 70 M_{\odot}$ that stands out (see, e.g., Fig. 3). These stars do not fit in the birthline constructed by considering a mass accretion rate in the star formation phase one order of magnitude lower than traditionally considered (see the green and red solid lines in Figs. 9 and 10, which correspond to 10^{-5} and $10^{-4} M_{\odot} \text{yr}^{-1}$, respectively). Beyond considering this result as a counterargument against this alternative scenario of massive star formation, it might also be interpreted as empirical evidence that these stars have followed a different (nonstandard) evolution. Some possibilities that have been proposed are binary interaction in general, mergers in particular, and/or chemically homogeneous evolution.

The first possibility is supported by recent findings indicating that a large portion of massive stars are born as part of a binary (and multiple) system. In most of the cases, binary interaction is expected to critically affect their evolution (Sana et al. 2012; Wang et al. 2020).

Binary-evolution models predict that a large portion of close binaries may exchange mass before they leave the MS (e.g., de Mink et al. 2013), with cases where the secondary mass has been increased, which produces a brighter star than any of the pre-interaction stars at a coeval age. This mass-transfer effect might lead to a secondary sample of stars that appear rejuvenated and with higher surface temperatures than the remaining stars that belong to the same cluster (Schneider et al. 2014; Wang et al. 2020).

Another possibility is that in extreme cases, some interacting binary systems might evolve into a configuration where both stars overflow their Roche lobes and eventually produce a merger (Benson 1970; Wellstein et al. 2001; Pols 1994; Wellstein et al. 2001; de Mink et al. 2007, 2012, 2014). On average, the percentage of mergers expected to occur in a given population of massive MS stars has been estimated to stay in the order of 10% (Podsiadlowski et al. 1992; Eldridge et al. 2011).

Stars resulting from a merger are not only more massive and more luminous than any of the stars in the progenitor binary system (de Mink et al. 2013; Schneider et al. 2014, 2019), but they are also predicted to suffer from a rejuvenation process as a result of renewed content of fresh hydrogen gas that is mixed into the central burning regions (Glebbeek et al. 2013; de Mink et al. 2014). In this sense, mergers are expected to be observationally detected as blue stragglers, that is, stars that appear to be younger than the age of the cluster in which they reside and are therefore closer to the ZAMS (e.g., Sills et al. 2002; Glebbeek et al. 2008; Mermilliod 1982; Chen & Han 2009; Lu et al. 2010).

The two channels indicated above might help to explain the presence of stars in the top left region of our empirical sHRD in the context of the lower accretion rate scenario; however, it might be argued that the same process is expected to lead to a similar filling of the gap region. One possible explanation to overcome this caveat might be that as indicated by Langer et al. (2019), only the stars above a certain mass have a phase where the envelope inflates and leads to a merger instead of the star-star mass transfer. In this context, it is also interesting to note that the

relative percentage of SB2 systems identified in our sample of 160 O dwarfs (see Fig. 4) in which the primary component has a mid-O spectral type is much higher than when the primary is an early O-type star. While not necessarily a definitive solution, we consider that this line of argument deserves a more in-depth study in the future.

An alternative or complementary explanation is the so-called chemically homogeneous evolution. Massive stars that reach a very high rotation rate (either during the star formation process or by angular momentum transfer in a binary system) are predicted to follow a peculiar evolution, evolving left- and upward in the HR diagram (Maeder 1987; de Mink et al. 2010; Brott et al. 2011).

Martins et al. (2013) showed empirical evidence of chemically homogeneous evolution taking place in environments with metallicity up to solar; however, this study was based on the investigation of a sample of early-type H-rich WN stars. Although several authors have reported observational support for it in sub-solar metallicity (Bouret et al. 2003; Walborn et al. 2004; Bouret et al. 2013), these studies are just based on a few targets, and similar findings have not been reported yet at solar metallicity. While more work is also needed in this direction (including the identification of peculiar nitrogen and helium surface abundance patterns in the very early O-type stars, see e.g., Rivero González et al. 2012), it is interesting to note that the early-O stars in our sample do not have extreme values of $v \sin i$ (Holgado 2019), as is required by massive stars to follow this type of evolution (Maeder 1987).

6. Summary and conclusions

The main conclusion that can be highlighted from this study is that the lack of O-type stars detectable in optical wavelengths and with parameters compatible with the theoretical ZAMS is a real and robust empirical fact. We summarize below the main line of work we have followed to reach this conclusion, and some other implications of this finding.

We performed a spectroscopic study of a sample of 415 Galactic O-type stars, implying 5-10 times stars more than any previous similar study in the literature. We showed that this sample is a good representation, in terms of spectral type and luminosity class, of the list of stars included in version 4.1 of the Galactic O star catalog, comprising $\sim 70\%$ of the stars quoted there. For most luminosity classes, the completeness (with respect to GOSC v4.1) approaches 75%. For the dwarf sample, this number is slightly smaller (60%). We demonstrated that our sample is not significantly affected by any systematic observational bias with respect to the GOSC sample (in particular, regarding stars with mid-O spectral types, corresponding to the region where the lack of stars close to the ZAMS is more pronounced). We consider that the sample is not clearly biased either for stars that are relatively extinguished by surrounding material from the associated parental cloud, although additional exploration is possible. We therefore suggest that any further attempt to confirm the existence of stars that are located closer to the theoretical ZAMS (in the mid-O spectral type range) than our sample of stars must imply the use of infrared observations, which can penetrate thicker layers of material and dust.

We performed a homogeneous quantitative spectroscopic analysis of 285 of the 415 stars in our initial sample (including likely single and SB1 stars, and excluding SB2 systems and a few stars with peculiar spectroscopic features), and located them in the Kiel and spectroscopic HR diagrams. We also collected and presented in the sHR diagram information from another ten

studies from the literature performing quantitative spectroscopy of Galactic O-type stars, based on different methods and stellar atmosphere codes. The shortage of O stars near the ZAMS prevails, and therefore we discarded any particular deficiency of our analysis strategy as the origin of the mismatch between observations and theory. A potential, more general, shortcoming in current stellar atmosphere codes, related to not considering the effect of turbulent pressure in the computation of the stellar atmosphere structure, and which could help to populate the gap region, was also briefly discussed.

We performed a more in-depth study of one of the youngest known Galactic clusters for which we have available high-resolution spectra: Trumpler-14. Compared with the GOSC catalog, we find that we do not lack decisive stars to cover the unpopulated area. We then constructed the HR diagram of the Trumpler-14 sample using *Gaia*-DR2 data. We evaluated the distribution of the sample and compared it with the analogous sHR diagram that we used. The general results are similar in both diagrams: equivalent area covered, and a lack of mid-O-type stars near the ZAMS. In addition, when we assumed a mass for the cluster as inferred from previous studies, the number of O stars that we assigned to Trumpler-14 is practically complete, and a large number of additional O stars belonging to that cluster are not expected.

The empirical evidence presented here for the existence of a gap close to the theoretical ZAMS represents (if not refuted by future observations) an important challenge for our current theories about the formation and evolution of massive stars. When we expand on this idea, in the case of high-mass stars, the theoretical ZAMS (which is based on instantaneous hydrogen ignition at a given mass) might be a different concept from the observed ZAMS, which is located at cooler effective temperatures and is related to the accretion timescale (i.e., the mass-accretion rate). In this sense, the hotter envelope of the observed distribution of O-type stars might trace a type of stellar birthline, as in the case of cooler stars, but this time, after starting the ignition of hydrogen in their cores.

In this line of argument, the variation in mass-accretion rate during star formation is a parameter that might help to explain the lack of empirically detected O-type stars close to the theoretical ZAMS. While the commonly assumed hypothesis of an accretion rate that is constant or increases with the mass of the accretor is not able to reproduce the empirical data, we showed that a decreasing rate of accretion with mass (turning from $\sim 10^{-4}$ to $\sim 10^{-5} M_{\odot}/\text{year}$ at $\sim 25 M_{\odot}$) might reconcile observations, evolutionary models, and hydrodynamical simulations.

A possible caveat to this proposal are the few O2–O3.5 dwarfs that are found much closer to the ZAMS than the remaining stars in our sample. However, this result might also be interpreted as empirical evidence indicating that this population of early O-type stars have experienced binary interaction, are the products of a stellar merger event, and/or are following a chemically homogeneous evolution. Although we cannot yet reach firm conclusions with the information presented in this paper, we propose that this line of argument deserves a more in-depth study in the future. In these regards, including in the investigated sample multi-epoch observations of all known early-type stars⁸ will allow us to obtain more statistically significant conclusions.

Acknowledgements. We express our extreme gratitude to the referee for the time devoted as their comments really contributed to improve this work.

⁸ For example, the ~ 15 stars in NGC 3603 with spectral types in the range O3–O3.5 identified by Melena et al. (2008), which are not included in our current sample due to their magnitude.

GH wants to thank J.Puls for his helpful comments and precise corrections that improved this manuscript significantly. GH acknowledges that this research has been partially funded by the Spanish State Research Agency (AEI) Project No. ESP2017-87676-C5-1-R and No. MDM-2017-0737 Unidad de Excelencia “María de Maeztu”- Centro de Astrobiología (INTA-CSIC). S-SD, DJL, and AHD acknowledge support from the Spanish Government Ministerio de Ciencia, Innovación y Universidades through grants PGC-2018-091 3741-B-C22, and from the Canarian Agency for Research, Innovation and Information Society (ACIISI), of the Canary Islands Government, and the European Regional Development Fund (ERDF), under grant with reference ProID2017010115. LH and GM thanks the Swiss National Science Foundation (project number 200020-172505). GM has received funding from the European Research Council (ERC) under the European Union’s Horizon 2020 research and innovation program (grant agreement No 833925). Based on observations made with the Nordic Optical Telescope, operated by NOTSA, and the Mercator Telescope, operated by the Flemish Community, both at the Observatorio del Roque de los Muchachos (La Palma, Spain) of the Instituto de Astrofísica de Canarias. Based on observations at the European Southern Observatory in programs 073.D-0609(A), 077.B-0348(A), 079.D-0564(A), 079.D-0564(C), 081.D-2008(A), 081.D-2008(B), 083.D-0589(A), 083.D-0589(B), 086.D-0997(A), 086.D-0997(B), 087.D-0946(A), 089.D-0975(A). This work has made use of data from the European Space Agency (ESA) mission *Gaia* (<https://www.cosmos.esa.int/gaia>), processed by the *Gaia* Data Processing and Analysis Consortium (DPAC, <https://www.cosmos.esa.int/web/gaia/dpac/consortium>). Funding for the DPAC has been provided by national institutions, in particular the institutions participating in the *Gaia* Multilateral Agreement.

References

- Alexander, M. J., Hanes, R. J., Povich, M. S., & McSwain, M. V. 2016, *AJ*, 152, 190
- Amores, E. B. & Lepine, J. R. D. 2004, in *Astronomical Society of the Pacific Conference Series*, Vol. 317, *Milky Way Surveys: The Structure and Evolution of our Galaxy*, ed. D. Clemens, R. Shah, & T. Brainerd, 317
- Arenou, F., Luri, X., Babusiaux, C., et al. 2018, *A&A*, 616, A17
- Arias, J. I., Walborn, N. R., Simón Díaz, S., et al. 2016, *AJ*, 152, 31
- Asplund, M., Grevesse, N., & Sauval, A. J. 2005, in *Astronomical Society of the Pacific Conference Series*, Vol. 336, *Cosmic Abundances as Records of Stellar Evolution and Nucleosynthesis*, ed. I. Barnes, Thomas G. & F. N. Bash, 25
- Bailer-Jones, C. A. L., Rybizki, J., Fouesneau, M., Mantelet, G., & Andrae, R. 2018, *AJ*, 156, 58
- Baraffe, I., Chabrier, G., & Gallardo, J. 2009, *ApJ*, 702, L27
- Baraffe, I., Vorobyov, E., & Chabrier, G. 2012, *ApJ*, 756, 118
- Barbá, R. H., Gamen, R., Arias, J. I., & Morrell, N. I. 2017, in *IAU Symposium*, Vol. 329, *The Lives and Death-Throes of Massive Stars*, ed. J. J. Eldridge, J. C. Bray, L. A. S. McClelland, & L. Xiao, 89–96
- Behrend, R. & Maeder, A. 2001, *A&A*, 373, 190
- Benson, R. S. 1970, in *BAAS*, Vol. 2, 295
- Berlanas, S. R., Wright, N. J., Herrero, A., Drew, J. E., & Lennon, D. J. 2019, *MNRAS*, 484, 1838
- Bernasconi, P. A. & Maeder, A. 1996, *A&A*, 307, 829
- Bouret, J. C., Hillier, D. J., Lanz, T., & Fullerton, A. W. 2012, *A&A*, 544, A67
- Bouret, J. C., Lanz, T., Hillier, D. J., et al. 2003, *ApJ*, 595, 1182
- Bouret, J. C., Lanz, T., Martins, F., et al. 2013, *A&A*, 555, A1
- Brott, I., de Mink, S. E., Cantiello, M., et al. 2011, *A&A*, 530, A115
- Caballero-Nieves, S. M., Gies, D. R., Bolton, C. T., et al. 2009, *ApJ*, 701, 1895
- Castro, N., Fossati, L., Langer, N., et al. 2014, *A&A*, 570, L13
- Cazorla, C., Morel, T., Nazé, Y., et al. 2017, *A&A*, 603, A56
- Chen, X. & Han, Z. 2009, *MNRAS*, 395, 1822
- Conti, P. S. 1975, *Memoires of the Societe Royale des Sciences de Liege*, 9, 193
- Cunha, K., Hubeny, I., & Lanz, T. 2006, *ApJ*, 647, L143
- Damiani, F., Kluttsch, A., Jeffries, R. D., et al. 2017, *A&A*, 603, A81
- Davies, B. & Beasor, E. R. 2019, *MNRAS*, 486, L10
- Davies, B., Hoare, M. G., Lumsden, S. L., et al. 2011, *MNRAS*, 416, 972
- de Mink, S. E., Brott, I., Cantiello, M., et al. 2012, *Astronomical Society of the Pacific Conference Series*, Vol. 465, *Challenges for Understanding the Evolution of Massive Stars: Rotation, Binariness, and Mergers*, ed. L. Drissen, C. Robert, N. St-Louis, & A. F. J. Moffat, 65
- de Mink, S. E., Cantiello, M., Langer, N., & Pols, O. R. 2010, in *American Institute of Physics Conference Series*, Vol. 1314, *American Institute of Physics Conference Series*, ed. V. Kalogera & M. van der Sluys, 291–296
- de Mink, S. E., Langer, N., Izzard, R. G., Sana, H., & de Koter, A. 2013, *ApJ*, 764, 166
- de Mink, S. E., Pols, O. R., & Hilditch, R. W. 2007, *A&A*, 467, 1181
- de Mink, S. E., Sana, H., Langer, N., Izzard, R. G., & Schneider, F. R. N. 2014, *ApJ*, 782, 7
- Drew, J. E., Herrero, A., Mohr-Smith, M., et al. 2018, *MNRAS*, 480, 2109
- Drew, J. E., Monguió, M., & Wright, N. J. 2019, *MNRAS*, 486, 1034
- Eggenberger, P., Meynet, G., Maeder, A., et al. 2008, *Ap&SS*, 316, 43
- Ekström, S., Georgy, C., Eggenberger, P., et al. 2012, *A&A*, 537, A146
- Eldridge, J. J., Langer, N., & Tout, C. A. 2011, *MNRAS*, 414, 3501
- Gaia Collaboration, Brown, A. G. A., Vallenari, A., et al. 2018a, *A&A*, 616, A1
- Gaia Collaboration, Mignard, F., Klioner, S. A., et al. 2018b, *A&A*, 616, A14
- Garmany, C. D., Conti, P. S., & Chiosi, C. 1982, *ApJ*, 263, 777
- Georgy, C., Ekstrom, S., Granada, A., et al. 2013, *VizieR Online Data Catalog*, J/A+A/553/A24
- Girichidis, P., Federrath, C., Allison, R., Banerjee, R., & Klessen, R. S. 2012a, *MNRAS*, 420, 3264
- Girichidis, P., Federrath, C., Banerjee, R., & Klessen, R. S. 2011, *MNRAS*, 413, 2741
- Girichidis, P., Federrath, C., Banerjee, R., & Klessen, R. S. 2012b, *MNRAS*, 420, 613
- Glebbeek, E., Gaburov, E., Portegies Zwart, S., & Pols, O. R. 2013, *MNRAS*, 434, 3497
- Glebbeek, E., Pols, O. R., & Hurley, J. R. 2008, *A&A*, 488, 1007
- Grunhut, J. H., Wade, G. A., Neiner, C., et al. 2017, *MNRAS*, 465, 2432
- Haemmerlé, L., Eggenberger, P., Ekström, S., et al. 2019, *A&A*, 624, A137
- Haemmerlé, L., Eggenberger, P., Meynet, G., Maeder, A., & Charbonnel, C. 2016, *A&A*, 585, A65
- Haemmerlé, L., Eggenberger, P., Meynet, G., et al. 2017, *A&A*, 602, A17
- Hanson, M. M. 1998, in *Astronomical Society of the Pacific Conference Series*, Vol. 131, *Properties of Hot Luminous Stars*, ed. I. Howarth, 1–13
- Herbig, G. H. 1962, *ApJ*, 135, 736
- Herrero, A., Kudritzki, R. P., Vilchez, J. M., et al. 1992, *A&A*, 261, 209
- Herrero, A., Simon-Díaz, S., Najarro, F., & Ribas, I. 2007, in *Astronomical Society of the Pacific Conference Series*, Vol. 367, *Massive Stars in Interactive Binaries*, ed. N. St. -Louis & A. F. J. Moffat, 67
- Hillier, D. J. 2012, in *IAU Symposium*, Vol. 282, *From Interacting Binaries to Exoplanets: Essential Modeling Tools*, ed. M. T. Richards & I. Hubeny, 229–234
- Hillier, D. J. & Lanz, T. 2001, in *Astronomical Society of the Pacific Conference Series*, Vol. 247, *Spectroscopic Challenges of Photoionized Plasmas*, ed. G. Ferland & D. W. Savin, 343
- Hillier, D. J. & Miller, D. L. 1998, *ApJ*, 496, 407
- Holgado, G. 2019, PhD thesis, Universidad de La Laguna
- Holgado, G., Simón-Díaz, S., & Barbá, R. 2017, in *Highlights on Spanish Astrophysics IX*, 394–400
- Holgado, G., Simón-Díaz, S., Barbá, R. H., et al. 2018, *A&A*, 613, A65
- Hosokawa, T., Offner, S. S. R., & Krumholz, M. R. 2011, *ApJ*, 738, 140
- Hosokawa, T. & Omukai, K. 2009, *ApJ*, 691, 823
- Hosokawa, T., Yorke, H. W., & Omukai, K. 2010, *ApJ*, 721, 478
- Hubrig, S., Schöller, M., Kharchenko, N. V., et al. 2011, *A&A*, 528, A151
- Hubrig, S., Schöller, M., Schnerr, R. S., et al. 2008, *A&A*, 490, 793
- Humphreys, R. M. 1978, *ApJS*, 38, 309
- Hur, H., Sung, H., & Bessell, M. S. 2012, *AJ*, 143, 41
- Iglesias, C. A. & Rogers, F. J. 1996, *ApJ*, 464, 943
- Kroupa, P. 2001, *MNRAS*, 322, 231
- Kudritzki, R. P. 1980, *A&A*, 85, 174
- Kudritzki, R. P., Bresolin, F., & Przybilla, N. 2003, *ApJ*, 582, L83
- Kuhn, M. A., Hillenbrand, L. A., Sills, A., Feigelson, E. D., & Getman, K. V. 2019, *ApJ*, 870, 32
- Kuiper, R., Klahr, H., Beuther, H., & Henning, T. 2010a, *ApJ*, 722, 1556
- Kuiper, R., Klahr, H., Beuther, H., & Henning, T. 2010b, *ApJ*, 722, 1556
- Kuiper, R., Klahr, H., Beuther, H., & Henning, T. 2011, *ApJ*, 732, 20
- Langer, N. & Kudritzki, R. P. 2014, *A&A*, 564, A52
- Langer, N., Schürmann, C., Stoll, K., et al. 2019, *arXiv e-prints*, arXiv:1912.09826
- Larson, R. B. 1969, *MNRAS*, 145, 271
- Larson, R. B. 1972, *MNRAS*, 157, 121
- Larson, R. B. & Starfield, S. 1971, *A&A*, 13, 190
- Lennon, D. J., Evans, C. J., van der Marel, R. P., et al. 2018, *A&A*, 619, A78
- Lindgren, L., Hernández, J., Bombrun, A., et al. 2018, *A&A*, 616, A2
- Lu, P., Deng, L. C., & Zhang, X. B. 2010, *MNRAS*, 409, 1013
- Luri, X., Brown, A. G. A., Sarro, L. M., et al. 2018, *A&A*, 616, A9
- Maeder, A. 1987, *A&A*, 178, 159
- Mahy, L., Rauw, G., De Becker, M., Eenens, P., & Flores, C. A. 2015, *A&A*, 577, A23
- Maíz Apellániz, J. & Barbá, R. H. 2018, *A&A*, 613, A9
- Maíz Apellániz, J., Barbá, R. H., Simón-Díaz, S., et al. 2018, *A&A*, 615, A161
- Maíz Apellániz, J., Sota, A., Arias, J. I., et al. 2016, *ApJS*, 224, 4
- Maíz Apellániz, J., Sota, A., Morrell, N. I., et al. 2013, in *Massive Stars: From alpha to Omega*, 198

- Maíz Apellániz, J., Sota, A., Walborn, N. R., et al. 2011, in *Highlights of Spanish Astrophysics VI*, ed. M. R. Zapatero Osorio, J. Gorgas, J. Maíz Apellániz, J. R. Pardo, & A. Gil de Paz, 467–472
- Maíz Apellániz, J., Trigueros Páez, E., Negueruela, I., et al. 2019, *A&A*, 626, A20
- Marcolino, W. L. F., Bouret, J. C., Martins, F., et al. 2009, *A&A*, 498, 837
- Markova, N., Puls, J., & Langer, N. 2018, *A&A*, 613, A12
- Markova, N., Puls, J., Simón-Díaz, S., et al. 2014, *A&A*, 562, A37
- Martins, F., Depagne, E., Russeil, D., & Mahy, L. 2013, *A&A*, 554, A23
- Martins, F., Donati, J. F., Marcolino, W. L. F., et al. 2010, *MNRAS*, 407, 1423
- Martins, F., Hervé, A., Bouret, J. C., et al. 2015, *A&A*, 575, A34
- Martins, F. & Plez, B. 2006, *A&A*, 457, 637
- Martins, F., Schaerer, D., & Hillier, D. J. 2005, *A&A*, 436, 1049
- Martins, F., Simón-Díaz, S., Barbá, R. H., Gamen, R. C., & Ekström, S. 2017, *A&A*, 599, A30
- Massey, P., Armandroff, T. E., Pyke, R., Patel, K., & Wilson, C. D. 1995a, *AJ*, 110, 2715
- Massey, P. & Johnson, J. 1993, *AJ*, 105, 980
- Massey, P., Lang, C. C., Degioia-Eastwood, K., & Garmany, C. D. 1995b, *ApJ*, 438, 188
- Massey, P., Neugent, K. F., Hillier, D. J., & Puls, J. 2013, *ApJ*, 768, 6
- Melena, N. W., Massey, P., Morrell, N. I., & Zangari, A. M. 2008, *AJ*, 135, 878
- Mermilliod, J. C. 1982, *A&A*, 109, 37
- Meyer, D. M.-A., Kuiper, R., Kley, W., Johnston, K. G., & Vorobyov, E. 2018, *MNRAS*, 473, 3615
- Morton, D. C. 1969, *ApJ*, 158, 629
- Nazé, Y., Walborn, N. R., & Martins, F. 2008, *Rev. Mexicana Astron. Astrofis.*, 44, 331
- Nelan, E. P., Walborn, N. R., Wallace, D. J., et al. 2010, *AJ*, 139, 2714
- Norberg, P. & Maeder, A. 2000, *A&A*, 359, 1025
- Palla, F. & Stahler, S. W. 1990, *ApJ*, 360, L47
- Palla, F. & Stahler, S. W. 1992, *ApJ*, 392, 667
- Peters, T., Banerjee, R., Klessen, R. S., & Mac Low, M.-M. 2011, *ApJ*, 729, 72
- Peters, T., Banerjee, R., Klessen, R. S., et al. 2010a, *ApJ*, 711, 1017
- Peters, T., Klessen, R. S., Mac Low, M.-M., & Banerjee, R. 2010b, *ApJ*, 725, 134
- Peters, T., Mac Low, M.-M., Banerjee, R., Klessen, R. S., & Dullemond, C. P. 2010c, *ApJ*, 719, 831
- Platais, I., Lennon, D. J., van der Marel, R. P., et al. 2018, *AJ*, 156, 98
- Podsiadlowski, P., Joss, P. C., & Hsu, J. J. L. 1992, *ApJ*, 391, 246
- Pols, O. R. 1994, *A&A*, 290, 119
- Puls, J., Urbaneja, M. A., Venero, R., et al. 2005, *A&A*, 435, 669
- Repolust, T., Puls, J., & Herrero, A. 2004, *A&A*, 415, 349
- Rivero González, J. G., Puls, J., Massey, P., & Najarro, F. 2012, *A&A*, 543, A95
- Sabín-Sanjulián, C., Simón-Díaz, S., Herrero, A., et al. 2017, *A&A*, 601, A79
- Sabín-Sanjulián, C., Simón-Díaz, S., Herrero, A., et al. 2014, *A&A*, 564, A39
- Sana, H., de Mink, S. E., de Koter, A., et al. 2012, *Science*, 337, 444
- Sana, H. & Evans, C. J. 2011, in *IAU Symposium, Vol. 272, Active OB Stars: Structure, Evolution, Mass Loss, and Critical Limits*, ed. C. Neiner, G. Wade, G. Meynet, & G. Peters, 474–485
- Sana, H., Le Bouquin, J. B., De Becker, M., et al. 2011, *ApJ*, 740, L43
- Sana, H., Momany, Y., Gieles, M., et al. 2010, *A&A*, 515, A26
- Santolaya-Rey, A. E., Puls, J., & Herrero, A. 1997, *A&A*, 323, 488
- Schaller, G., Schaerer, D., Meynet, G., & Maeder, A. 1992, *A&AS*, 96, 269
- Schneider, F. R. N., Izzard, R. G., de Mink, S. E., et al. 2014, *ApJ*, 780, 117
- Schneider, F. R. N., Ohlmann, S. T., Podsiadlowski, P., et al. 2019, *Nature*, 574, 211
- Schneider, F. R. N., Ramírez-Agudelo, O. H., Tramper, F., et al. 2018, *A&A*, 618, A73
- Siess, L., Forestini, M., & Bertout, C. 1997, *A&A*, 326, 1001
- Sills, A., Adams, T., Davies, M. B., & Bate, M. R. 2002, *MNRAS*, 332, 49
- Simón-Díaz, S., Caballero, J. A., Lorenzo, J., et al. 2015a, *ApJ*, 799, 169
- Simón-Díaz, S., Castro, N., Garcia, M., Herrero, A., & Markova, N. 2011, *Bulletin de la Societe Royale des Sciences de Liege*, 80, 514
- Simón-Díaz, S., Godart, M., Castro, N., et al. 2017, *A&A*, 597, A22
- Simón-Díaz, S. & Herrero, A. 2014, *A&A*, 562, A135
- Simón-Díaz, S., Herrero, A., Sabín-Sanjulián, C., et al. 2014, *A&A*, 570, L6
- Simón-Díaz, S., Negueruela, I., Maíz Apellániz, J., et al. 2015b, in *Highlights of Spanish Astrophysics VIII*, 576–581
- Smith, N. 2006, *MNRAS*, 367, 763
- Stahler, S. W. 1983, *ApJ*, 274, 822
- Stahler, S. W. 1988, *ApJ*, 332, 804
- Tognelli, E., Prada Moroni, P. G., & Degl’Innocenti, S. 2015, *MNRAS*, 454, 4037
- Vanbeveren, D., De Loore, C., & Van Rensbergen, W. 1998, *A&A Rev.*, 9, 63
- Wade, G. A., Howarth, I. D., Townsend, R. H. D., et al. 2011, *MNRAS*, 416, 3160
- Walborn, N. R. 1972, *AJ*, 77, 312
- Walborn, N. R. 1973a, *ApJ*, 179, 517
- Walborn, N. R. 1973b, *AJ*, 78, 1067
- Walborn, N. R. 2009, *Optically observable zero-age main-sequence O stars*, ed. M. Livio & E. Villaver, 167–177
- Walborn, N. R. & Blades, J. C. 1997, *ApJS*, 112, 457
- Walborn, N. R., Morrell, N. I., Howarth, I. D., et al. 2004, *ApJ*, 608, 1028
- Walborn, N. R. & Parker, J. W. 1992, *ApJ*, 399, L87
- Wang, C., Langer, N., Schootemeijer, A., et al. 2020, *ApJ*, 888, L12
- Wellstein, S., Langer, N., & Braun, H. 2001, *A&A*, 369, 939
- Williams, A. M., Gies, D. R., Bagnuolo, W. G., J., et al. 2001, *ApJ*, 548, 425
- Yorke, H. W. 1986, *ARA&A*, 24, 49

Appendix A: HD199579: an O6.5 Vz star within the gap region?

The only star that is located within the gap region in Fig. 5 (according to the parameters determined by Martins et al. 2015) is HD 199579, a double-line spectroscopic binary including a dominant O6.5 Vz main component and a very faint companion (Williams et al. 2001). Martins et al. performed a spectroscopic analysis of a high-resolution optical spectrum of the star with the CMFGEN code (Hillier & Miller 1998; Hillier & Lanz 2001; Hillier 2012) and found $T_{\text{eff}} = 41\,500$ K, $\log g_{\text{true}} = 4.15$ dex). Our analysis for this star provides quite different values ($T_{\text{eff}} = 39.5 \pm 0.8$ kK, $\log g_{\text{true}} = 3.9 \pm 0.1$ dex), however. As an exercise to evaluate to which extent the parameters provided by Martins et al. can be considered a valid solution from the IACOB-GBAT/FASTWIND analysis, we launched the tool again, but forcing the surface gravity to a value closer to that expected in the ZAMS (and close to the one obtained by Martins et al. 2015), that is, $\log g = 4.2$ dex. The results are shown in Fig A.1 and prove that when the surface gravity is forced to a higher value, the associate FASTWIND best-fitting model is not able to fit the wings of the H δ and He II $\lambda 4541$ lines accurately. Further inspection of the bottom panel of Fig. A.1 indicates that this set of parameters obtained by Martins et al. is well above the 3σ tolerance level of the χ^2 -fitting. We note that the difference in surface gravity is beyond the ~ 0.10 – 0.15 dex systematic difference that has been claimed to be present between the FASTWIND and CMFGEN codes (Massey et al. 2013; Holgado et al. 2018).

Another possible explanation for the disagreement in the derived parameters of HD 199579 is that we did not analyze the same spectrum as Martins et al. (2015). The multi-epoch character of the IACOB survey allows us to perform an academic exercise to check this possibility by analyzing the 119 available spectra. The resulting values and uncertainties are presented in Fig. A.2, sorted according to the radial velocity measurement of each spectrum (we recall that HD 199579 is an SB2 system in which the secondary is much fainter than the primary, and that it is therefore not easily detected in the individual spectra). All our measurements are within the grid-step in $\log g$ of ± 0.1 dex, and far away from the gravity estimated by Martins et al. (2015) (and the one expected for the star to be on the ZAMS).

Therefore it is not evident that the result of Martins et al. (2015) for HD 199579 can be considered as a critical counterexample of the absence of O-type stars near the ZAMS. Even considering the parameters derived by Martins et al. (2015), given the fact that this is the only star located within the gap, the scarcity of stars in this region is still a remarkable empirical result.

Appendix B: Membership and distance of Trumpler-14

Based on the discussion in Sect. 5.3, it is clear that due to its extreme youth, ≤ 1 Myr, Trumpler-14 is critical in verifying the reality of the observed gap in the sHRD because the presence or absence of mid-O dwarfs close to the ZAMS in such a young cluster is a very strong constraint. Determining cluster membership of Trumpler-14 is therefore extremely important, and while the distribution of stars in the sHRD does not depend on distance, this is relevant for deciding whether individual stars are cluster members. As pointed out in Sect. 5.3, the mutual proximity of the clusters Trumpler-14 and Trumpler-16 has resulted in some confusion regarding cluster membership. For example, the stars or stellar systems HD 93161, HD 93160 and HD 93250

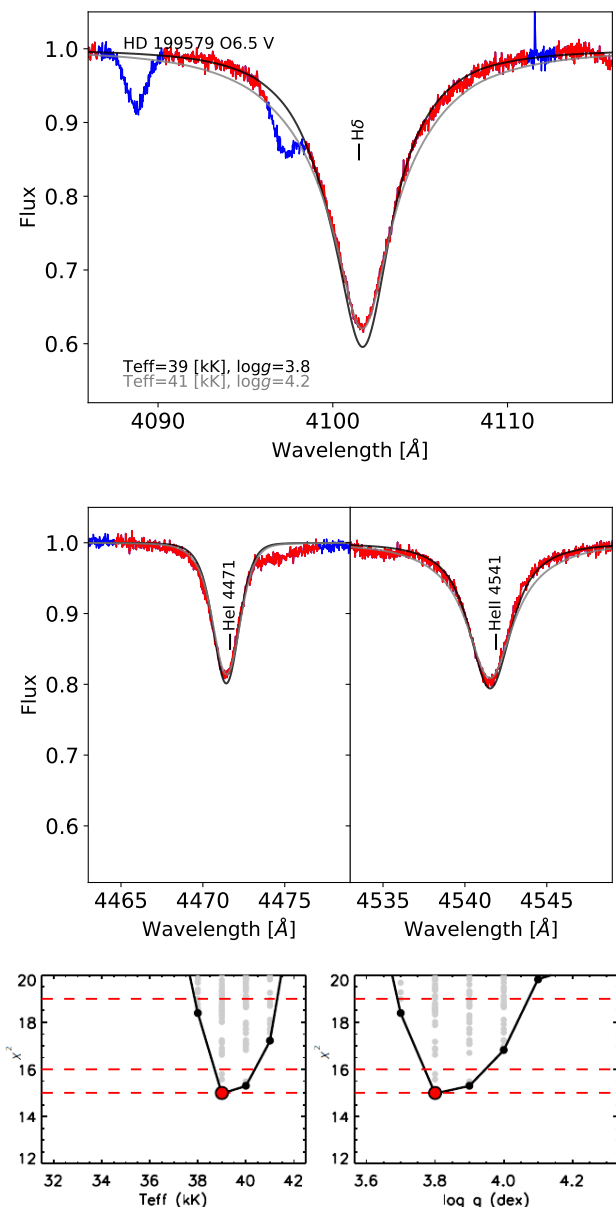


Fig. A.1: *Top and middle* Comparison of the synthetic spectra of two best-fitting FASTWIND models to the observed spectrum of the O6.5 Vz star HD 199579 for three diagnostic lines. The first best-fitting model corresponds to the IACOB-GBAT analysis with T_{eff} and $\log g$ as free parameters (the red part is fitted and the blue part is ignored). In the second model, $\log g$ was fixed to 4.2 dex. *Bottom* χ^2 distributions for T_{eff} and $\log g$ resulting from the IACOB-GBAT analysis. The horizontal dashed lines represent the value of χ^2 for the best-fitting model (red dots) and the 1σ and 2σ confidence levels. Any model with $\log g \sim 4.2$ is clearly beyond the 2σ level.

are sometimes attributed to Trumpler-16 even though they are close to Trumpler-14, see, for example, the discussion in Walborn (1973a) and Smith (2006). However, as noted in these papers (see also Hur et al. (2012)), these clusters have very similar distances such that separating individual stars on the basis of their distance would appear to be difficult. We therefore used *Gaia*-DR2 data (Lindgren et al. 2018) to investigate clus-

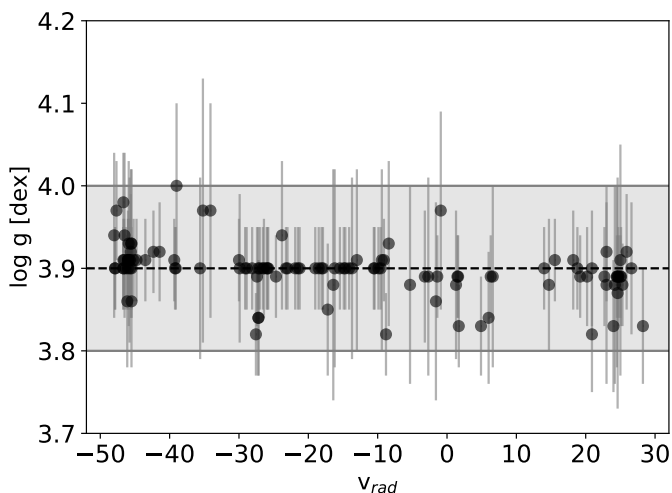


Fig. A.2: Results from the IACOB-GBAT analysis (regarding $\log g$) of 119 multi-epoch spectra of the SB2 star HD 199579, sorted according to the radial velocity of the spectrum. Uncertainties from the analyses are included as vertical error bars. The uncertainty in the original analysis in $\log g$ (± 0.1 dex) is shown as a gray area around the value obtained there, which is also the median value of all estimates ($\log g = 3.9$ dex).

ter membership probabilities based on distance and proper motion, as discussed below.

We extracted all $\sim 150\,000$ sources within $30'$ of the center of Trumpler-16. This region includes Trumpler-14 and also Trumpler-15, a rather older cluster several arcminutes north of Trumpler-14. The region also hosts stars belonging to other potential comoving groups such as Collinder 228 and 232. Because of their sparsity and the debate about their reality as physical groups, discussed by Walborn (1973b) and Smith (2006), we do not discuss these further in this paper. We applied the following filters to these sources: $\text{pmra_error} < 0.07$ mas/yr, $\text{pmdec_error} < 0.07$ mas/yr, $0.3 < \text{parallax} < 0.5$ mas, and $\text{bp_rp} < 1.2$. The restrictions on proper motion are prompted by the discussion of outliers in the crowded regions of 30 Dor by Lennon et al. (2018) (see also Platais et al. 2018), while the color cut was used to exclude red giants. The color restriction also excludes massive stars that have intrinsic high extinction (known to exist in the region), but we note that the objective here is not to derive a complete list of cluster members, but rather to define secure cluster members. In this context, for the clusters in question, we defined as candidates all sources within $5'$ of the cluster centers (as defined in Table B.1) and removed outliers in both proper motion directions with a 2σ clipping algorithm. The results for the mean parallax and proper motion quantities are listed in Table B.1. They agree excellently with results from other estimates from *Gaia* data, but using a different method (e.g., Kuhn et al. 2019, who also discussed the cluster internal dynamical properties).

The mean parallaxes of the two clusters are identical to within 3σ , having a value of 0.39 mas, to two significant figures. Correcting for the systematic error in the *Gaia* zero-point of 0.03 mas, but ignoring the uncertainty associated with the spatially correlated error term (see discussion in subsection 5.4 of Lindegren et al. 2018), implies a mean parallax of 0.42 ± 0.05 mas, or a distance of 2.38 kpc, with an uncertainty of about 10%. This agrees very well with the η Car geometric distance of 2.35 ± 0.05

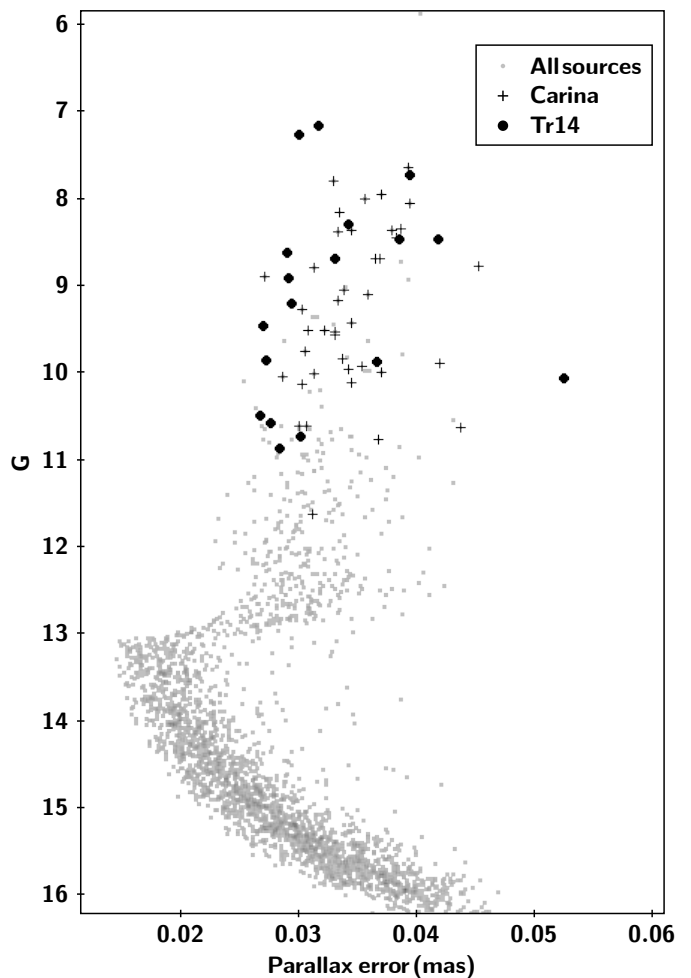


Fig. B.1: *Gaia* G magnitude vs. parallax error. The gray points represent sources in the Trumpler-14, 15, and 16 region according to the selection criteria discussed in the text, while the black points (see inset for key) are the measurements for the bright OWN O-type stars in Carina and our Trumpler-14 candidate O-type stars.

kpc (Smith 2006). In Fig.B.1 we show the dependence of the parallax errors on magnitude, to be compared with Fig. B.2 of Lindegren et al. (2018). The bright O-stars of interest here typically have parallax errors in the range 0.03 to 0.05 mas. Therefore distances to individual stars cannot be used to help define cluster membership, and we turn accordingly to the differences in proper motion between Trumpler-14 and Trumpler-16.

We illustrate the proper motions in Figure B.2, where we also show the proper motions of our candidate O-stars in Trumpler-14. The region clearly is dynamically quite complex, with significant substructure. Nevertheless, based on the similarity of Trumpler-14 and Trumpler-15 mean proper motions, we can assign them to the same broad dynamical group, distinct from the Trumpler-16 group (which is clearly also part of a larger dynamical group extending to the upper left corner of Figure B.2). We note here in passing that the anonymous group to the lower right in this figure consists of a comoving though spatially diffuse group of massive stars at the same distance as the other clusters.

While there are some significant outliers within the Trumpler-14 candidates to which we return below, the critical mid-O dwarf stars HDE 303311, CPD-58 2611, Tr 14-9,

Table B.1: Mean parallax and proper motion estimates for Trumpler-14, 15, and 16, as discussed in Appendix A.

Cluster Name	Field centers		number of stars	Parallax mas	pmRA mas yr ⁻¹	pmDEC mas yr ⁻¹
	RA	DEC				
Trumpler-14	160.957	-59.568	98	0.39 ± 0.03	-6.599 ± 0.227	1.980 ± 0.156
Trumpler-15	161.167	-59.363	92	0.39 ± 0.04	-6.185 ± 0.209	2.048 ± 0.107
Trumpler-16	161.236	-59.720	102	0.39 ± 0.04	-6.985 ± 0.153	2.591 ± 0.108

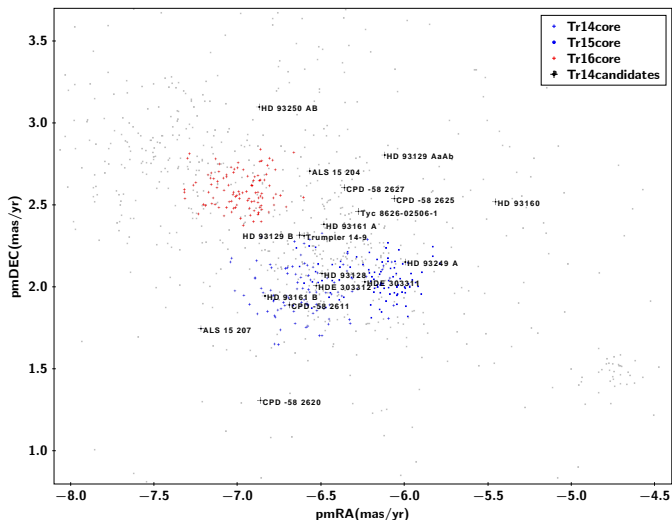


Fig. B.2: Gray symbols are the proper motions of all sources that meet our filter criteria around the core Trumpler-14, 15, and 16 regions. The colored symbols represent the core dynamical groups as discussed in the text (see inset for key), after 2σ clipping. Overplotted are the proper motions of our candidate O-stars in Trumpler-14 (see Table 1). The two labels that overlap and are difficult to read are for the stars HD 93129B and Trumpler-14-9.

HD 93161A, and HD 93161B (cf. Table 1) are all securely within the Trumpler-14 and 15 group. HD 93128 (an O3.5 V((f))z) is a common Trumpler-14 member from the Gaia data, slightly more massive than the mid-O dwarfs crucial to the gap, and a member of the more massive stars that appear closer to the ZAMS. The spectroscopic binary HD 93160AB is rather discrepant, but it is in any case classified as O7 III((f)). Its proper motion is even more inconsistent with Trumpler-16 membership, however (its proper motion vector is almost orthogonal to the Trumpler-16 proper motion relative to Trumpler-14). The proper motion of HD 93219AaAb is also rather different from the two dynamical groups. In this case, however, we note that Nelan et al. (2010) used HST/FGS to separate this system into two components separated by 53 ± 3 mas and 0.9 ± 0.05 magnitudes. Therefore it is quite possible that the closeness and comparable magnitudes of the components have affected the Gaia astrometry and proper motion measurement (Lennon et al. 2018). Finally, of the outliers we discuss here, we note that while HD 93250 has also been separated into two components of almost equal magnitude (Sana et al. 2011), with separation 1.5 ± 0.2 mas, its proper motion is similar to that of Trumpler-16, and it is likely a member of that cluster.

Appendix C: Stellar tracks from stellar models in which the accretion rate was altered

In reference to the evolutionary models used in the Sect. 5.4.1, we include here some of the characteristics that defines them. The Geneva stellar evolution code is a one-dimensional hydrostatic code that numerically solves the structure equations with the Henyey method. The code includes energy production by gravitational contraction and nuclear reactions, including hydrogen-, lithium-, deuterium-, and all the hydrostatic burning phases until the core Si-burning phases. Opacities are interpolated from the OPAL tables (Iglesias & Rogers 1996), and convection is treated with the mixing-length theory and the Schwarzschild criterion. A detailed description of the code without accretion is available in Eggenberger et al. (2008).

The treatment of accretion is described in detail in Haemmerlé et al. (2016). Here we recall only the main ingredients. The accretion rate is a free parameter. The accreted material is added at each time step at the surface of the star. Its thermal properties are set to be identical to that of the stellar surface (cold-disk accretion). This assumption corresponds to a disk-like accretion geometry, in which any entropy excess is radiated away in the polar directions before it is advected in the stellar interior. This is a lower limit for the accretion of entropy that leads during the early accretion phase to smaller stellar radii than any other assumption. However, the differences in radii between hot and cold accretion disappear as the star reaches the ZAMS (ignition point), so that we do not expect this assumption to affect the results of our study.

The main characteristics of the models used are included in Table C.1. We first consider constant accretion rates of $\dot{M} = 10^{-5} - 10^{-4} - 10^{-3} M_{\odot} \text{ yr}^{-1}$. For $\dot{M} = 10^{-5} - 10^{-4} M_{\odot} \text{ yr}^{-1}$, the runs start at $0.7 M_{\odot}$. However, accretion at high rate on low-mass objects makes numerical convergence difficult to achieve. For $\dot{M} = 10^{-3} M_{\odot} \text{ yr}^{-1}$ we therefore start the computation at $2 M_{\odot}$. In all the cases, the initial protostellar seed is a fully convective hydrostatic object located at the top of the Hayashi line corresponding to its mass. All the accreting models run until they reach a final mass of $M = 70 M_{\odot}$. For the chemical composition, we use solar abundances ($Z=0.014$, Asplund et al. 2005; Cunha et al. 2006) in the initial model and the accreted material. In order to distinguish between the observational constraints on the various mass ranges, we compute in addition models with initial accretion rates identical to those described above, but switched to a different value when the stellar mass reaches $25 M_{\odot}$. A detailed description of the internal and surface properties of the models at constant rates is available in Haemmerlé et al. (2016).

Appendix D: Proxy shape of the gap

As a quick method to favor comparisons with our resulting gap near the ZAMS, we designed a polyhedron using specific points of the evolutionary tracks in the sHRD (Fig. 3) surrounding the region. Table D.1 includes the parameters that define the models at these points for the sHRD. We then transferred the shape to

Table C.1: Geneva evolutionary models with controlled mass-accretion rate used here

Name	\dot{M}_{init} [$M_{\odot} \text{ yr}^{-1}$]	$\dot{M}_{>25M_{\odot}}$ [$M_{\odot} \text{ yr}^{-1}$]	Draw
Model1	10^{-5}	10^{-5}	Fig. 9 (green)
Model2	10^{-5}	10^{-4}	Fig. 9 (red)
Model3	10^{-4}	10^{-4}	Fig. 10 (red)
Model4	10^{-4}	10^{-5}	Fig. 10 (green)
Model5**	10^{-3}	10^{-3}	Fig. 11 (blue)
Model6**	10^{-3}	10^{-5}	Fig. 11 (green)

Initial mass: $0.7 M_{\odot}$. (** $2 M_{\odot}$). Final mass: $70 M_{\odot}$.
Z=0.014

Table D.1: Parameter model values to define a proxy of the shape of the gap near the ZAMS

Mass at ZAMS [M_{\odot}]	$\log(T_{\text{eff}})$	$\log g$	$\log(\mathcal{L}/\mathcal{L}_{\odot})$	$\log(L/L_{\odot})$
25	4.59	4.28	3.47	4.86
30	4.60	4.10	3.69	5.19
60	4.65	3.97	4.01	5.76
85	4.71	4.19	4.05	5.98

the remaining diagrams (Kiel and HR) with the remaining parameter values for that model at the same point, also included in Table D.1.

Appendix E: Tables

Table E.1: List of the 285 stars with spectroscopic parameters obtained in this work. Stars are separated by luminosity class (horizontal lines) and sorted by spectral type. Columns are: (1, 2) Name and spectral type from GOSC, (3, 4, 5) T_{eff} , $\log g_{\text{true}}$ and $\log \mathcal{L}$ from this work (See notes on Holgado et al. 2018, for associated uncertainties), (6) B magnitude from GOSC, (7) the extinction measurement $E(4405\text{-}5495)$ from Maíz Apellániz & Barbá (2018), (8) additional notes.

Name	SpT LC	T_{eff} [kK]	$\log g_{\text{true}}$ [dex]	$\log \mathcal{L}/\mathcal{L}_{\odot}$ [dex]	B [mag]	$E(4405\text{-}5495)$	Notes
HD 93129 AaAb	O2 I f*	45.6±1.1	3.89±0.10	4.14±0.11	7.8	0.514	Weak He I lines; SB1
CYGOB2-7	O3 I f*	50.3±1.8	4.09±0.13	4.11±0.14	12.2	1.827	Weak He I lines
ALS 15210	O3.5 I f* Nwk	42.4±1.6	3.69±0.05	4.21±0.08	11.5	.	Weak He I lines
HD 190429 A	O4 I f	36.6±0.8	3.53±0.09	4.11±0.10	7.3	0.447	.
HD 15570	O4 I f	40.2±0.8	3.63±0.06	4.18±0.07	8.8	0.933	Weak He I lines
HD 16691	O4 I f	>39.7	>3.74	<4.05	9.1	0.742	Weak He I lines
HD 14947	O4.5 I f	39.1±1.1	3.65±0.10	4.11±0.11	8.5	0.689	.
CYGOB2-9	O4.5 I f	40.1±1.0	3.92±0.10	3.88±0.11	12.9	2.293	Weak He I lines
CPD -47 2963 AB	O5 I fc	37.1±0.5	3.51±0.04	4.16±0.05	9.7	1.168	.
HD 93632	O5 I f var	40.0±0.5	3.90±0.19	3.90±0.19	8.7	0.538	.
CYGOB2-11	O5.5 I fc	37.3±1.5	3.63±0.14	4.05±0.16	11.7	1.813	.
HD 169582	O6 I a f	38.9±1.3	3.70±0.21	4.05±0.22	9.3	0.786	.
HD 152233	O6 II (f)	37.8±0.5	3.69±0.04	4.01±0.05	6.8	0.383	SB1
HD 163758	O6.5 I a fp	34.6±0.6	3.29±0.07	4.26±0.08	7.3	0.277	.
CPD -26 2716	O6.5 I ab f	36.0±0.5	3.51±0.06	4.11±0.06	10.1	0.625	.
HD 172175	O6.5 I (n)fp	36.2±0.5	3.58±0.05	4.04±0.06	10.0	0.896	.
HD 157857	O6.5 II (f)	36.7±0.7	3.60±0.08	4.05±0.09	8.0	0.439	.
HD 210839	O6.5 I (n)fp	35.8±0.5	3.47±0.04	4.14±0.05	5.3	0.487	.
HD 151515	O7 II (f)	36.0±1.0	3.55±0.13	4.07±0.14	7.3	0.423	.
HD 193514	O7 Ib (f)	35.9±0.5	3.58±0.04	4.03±0.05	7.8	0.714	.
HD 69464	O7 Ib (f)	35.8±1.0	3.38±0.08	4.23±0.09	9.1	0.554	.
BD -13 4927	O7 II (f)	36.0±0.5	3.51±0.05	4.11±0.06	10.4	1.141	.
HD 94963	O7 II (f)	36.3±0.6	3.54±0.06	4.09±0.07	7.1	0.209	.
HD 120521	O7.5 Ib (f)	34.6±0.6	3.39±0.07	4.16±0.08	8.8	0.480	.
HD 171589	O7.5 II (f)	36.5±0.8	3.66±0.06	3.98±0.07	8.5	0.555	.
HD 17603	O7.5 Ib (f)	33.3±0.8	3.26±0.08	4.22±0.09	9.1	0.880	SB1
HD 156154	O7.5 Ib (f)	34.2±0.5	3.31±0.04	4.22±0.05	8.7	0.849	.
HD 192639	O7.5 I ab f	34.7±0.7	3.43±0.11	4.12±0.12	7.5	0.593	.
HD 188001	O7.5 I ab f	32.4±0.5	3.20±0.09	4.23±0.09	6.2	0.257	SB1
HD 34656	O7.5 II (f)	36.0±0.5	3.50±0.04	4.12±0.05	6.9	0.294	.
HD 96917	O8 Ib (n)(f)	32.0±0.5	3.20±0.04	4.21±0.05	7.2	0.330	.
HD 175754	O8 II (n)((f))p	34.2±0.5	3.39±0.04	4.14±0.05	6.9	0.184	.
HD 151804	O8 I a f	<28.2	2.86±0.05	4.33±0.05	5.3	0.317	.
HD 162978	O8 II ((f))	35.0±0.5	3.50±0.04	4.07±0.05	6.2	0.300	.
BD -11 4586	O8 Ib (f)	32.4±0.6	3.22±0.10	4.21±0.11	10.4	1.241	.
HD 225160	O8 I ab f	33.2±1.2	3.35±0.14	4.12±0.15	8.5	0.492	.
HD 75211	O8.5 II ((f))	33.4±0.6	3.40±0.06	4.08±0.07	7.9	0.653	SB1
HD 125241	O8.5 Ib (f)	32.1±0.5	3.24±0.04	4.18±0.05	8.8	0.723	.
HDE 303492	O8.5 I a f	28.3±1.0	2.91±0.06	4.29±0.09	9.4	0.790	.
BD +39 1328	O8.5 I ab (n)(f)	32.8±0.6	3.42±0.09	4.03±0.10	10.4	0.800	.
HD 112244	O8.5 I ab (f)p	31.5±0.7	3.23±0.11	4.15±0.12	5.4	0.267	SB1
HD 74194	O8.5 Ib-II (f)p	32.2±0.5	3.36±0.04	4.06±0.05	7.8	0.468	SB1
HD 207198	O8.5 II ((f))	33.1±0.5	3.31±0.04	4.16±0.05	6.3	0.579	.
HD 148546	O9 I ab	32.0±0.5	3.30±0.04	4.11±0.05	8.0	0.516	.
HD 155756	O9 Ib p	32.0±0.5	3.29±0.04	4.12±0.05	9.8	0.768	.
HD 151018	O9 Ib	32.0±0.5	3.31±0.04	4.10±0.05	9.3	0.860	.
HD 173783	O9 I ab	31.2±0.5	3.09±0.09	4.28±0.09	9.8	0.732	.
HD 191423	ON9 II-III nn	32.3±0.8	3.71±0.06	3.72±0.07	8.2	0.399	.
HD 71304	O9 II	32.0±0.5	3.30±0.04	4.11±0.05	8.8	0.766	.
HD 209975	O9 Ib	32.0±0.5	3.30±0.04	4.11±0.05	5.2	0.321	.
HD 210809	O9 I ab	30.9±0.5	3.12±0.05	4.23±0.06	7.6	0.289	.
HD 202124	O9 I ab	31.1±0.5	3.22±0.06	4.14±0.07	8.0	0.513	.
HD 152249	OC9 I ab	31.1±0.5	3.21±0.04	4.15±0.05	6.6	0.448	.

$$\mathcal{L} = T_{\text{eff}}^4 / g_{\text{true}}, \quad g_{\text{true}} = g + g_{\text{cent}}, \quad g_{\text{cent}} \approx \frac{(V_{\text{rot}} \sin i)^2}{R_*}$$

Table E.1: continued.

Name	SpT LC	T_{eff} [kK]	$\log g_{\text{true}}$ [dex]	$\log \mathcal{L}/\mathcal{L}_{\odot}$ [dex]	B [mag]	E(4405-5495)	Notes
HD 237211	O9 Ib	30.7±0.6	3.09±0.07	4.25±0.08	9.5	0.714	.
HD 30614	O9 Ia	29.4±0.6	3.00±0.07	4.26±0.08	4.3	0.262	SB1
CPD -59 5634	O9.2 Ib	31.8±0.5	3.28±0.04	4.12±0.05	10.3	0.988	.
HD 101545 AaAb	O9.2 II	31.9±0.5	3.37±0.06	4.04±0.07	7.5	0.273	.
HD 37742	O9.2 Ib Nwk var	30.1±0.5	3.15±0.04	4.15±0.05	1.9	.	SB1
HD 76968	O9.2 Ib	30.8±0.5	3.28±0.04	4.06±0.05	7.2	0.355	SB1
HD 123008	ON9.2 Iab	31.7±0.5	3.22±0.05	4.17±0.06	9.2	0.599	.
HD 154368	O9.2 Iab	30.4±0.5	3.04±0.04	4.28±0.05	6.6	0.733	.
HD 218915	O9.2 Iab	31.1±0.5	3.22±0.04	4.14±0.05	7.2	0.249	.
HD 152424	OC9.2 Ia	30.2±0.5	3.17±0.06	4.14±0.07	6.7	0.636	SB1
HD 36486 AaAb	O9.5 II Nwk	30.1±0.5	3.33±0.04	3.97±0.05	2.3	0.036	SB1
HD 188209	O9.5 Iab	30.1±0.5	3.04±0.09	4.26±0.09	5.6	0.151	.
HD 10125	O9.7 II	30.9±0.5	3.41±0.05	3.94±0.06	8.7	0.528	SB1
HD 89137	ON9.7 II (n)	29.1±0.5	3.37±0.03	3.88±0.04	7.9	0.192	.
HD 28446 A	O9.7 II n	29.8±0.5	3.65±0.05	3.64±0.06	6.0	0.396	.
HD 165174	O9.7 II n	30.2±0.8	3.45±0.08	3.86±0.09	6.1	0.206	SB1
HD 305619	O9.7 II	31.0±0.5	3.29±0.04	4.07±0.05	9.9	0.685	.
HD 75222	O9.7 Iab	30.2±0.5	3.22±0.05	4.09±0.06	7.8	0.601	.
HD 18409	O9.7 Ib	30.0±0.5	3.15±0.04	4.15±0.05	8.8	0.629	.
HD 173010	O9.7 Ia+ var	27.9±0.5	2.99±0.04	4.18±0.05	10.0	1.030	.
HD 152003	O9.7 Iab Nwk	30.1±0.5	3.18±0.06	4.12±0.07	7.4	0.601	.
HD 13745	O9.7 II (n)	30.0±0.5	3.29±0.05	4.01±0.06	8.0	0.393	.
HD 167264	O9.7 Iab	28.8±0.9	3.14±0.13	4.09±0.14	5.4	0.262	SB1
HD 105056	ON9.7 Ia e	27.4±0.6	2.88±0.08	4.26±0.09	7.4	.	.
HD 195592	O9.7 Ia	28.0±0.5	2.91±0.04	4.27±0.05	8.0	1.074	.
HD 149038	O9.7 Iab	29.8±0.5	3.18±0.04	4.11±0.05	5.0	0.285	.
HD 225146	O9.7 Iab	28.3±0.6	3.11±0.09	4.09±0.10	9.0	0.566	.
HD 104565	OC9.7 Iab	28.9±0.5	3.01±0.04	4.22±0.05	9.6	0.542	.
HD 191781	ON9.7 Iab	28.7±2.0	<3.39	>3.83	10.3	0.840	.
HD 154811	OC9.7 Ib	29.8±0.5	3.22±0.04	4.07±0.05	7.3	0.593	.
HD 152147	O9.7 Ib Nwk	30.1±0.5	3.26±0.09	4.04±0.09	7.8	0.615	SB1
HD 47432	O9.7 Ib	29.1±0.5	3.04±0.04	4.21±0.05	6.4	0.339	.
HD 68450	O9.7 II	30.6±0.9	3.31±0.13	4.02±0.14	6.4	0.229	.
HD 152405	O9.7 II	30.3±0.5	3.29±0.09	4.03±0.09	7.3	0.364	SB1
HD 93843	O5 III (fc)	37.3±0.6	3.53±0.05	4.15±0.06	7.3	0.247	.
HD 97253	O5 III (f)	39.1±0.5	3.60±0.04	4.16±0.05	7.4	0.423	.
HD 14442	O5 ... n(f)p	39.1±1.3	3.62±0.13	4.14±0.14	9.6	0.682	.
HDE 338 931	O6 III (f)	38.1±0.6	3.76±0.09	3.95±0.09	9.8	0.949	.
HD 156738 AB	O6.5 III (f)	37.9±1.1	3.83±0.15	3.87±0.16	10.6	1.175	.
HD 190864	O6.5 III (f)	37.5±0.9	3.64±0.08	4.05±0.09	8.0	0.460	.
HD 96946	O6.5 III (f)	39.0±0.5	3.86±0.07	3.89±0.07	8.7	0.487	.
HD 175876	O6.5 III (n)(f)	36.1±0.6	3.59±0.04	4.03±0.05	6.8	0.160	.
HD 130298	O6.5 III (n)(f)	38.2±0.6	3.69±0.06	4.03±0.07	9.7	0.674	SB1
HD 152723 AaAb	O6.5 III (f)	38.0±0.5	3.81±0.04	3.90±0.05	7.6	0.382	SB1
BD +60 2522	O6.5 ... (n)fp	36.2±1.1	3.55±0.14	4.07±0.15	9.1	0.668	.
HD 167659	O7 II-III (f)	37.0±0.5	3.60±0.04	4.06±0.05	7.6	0.484	.
HD 94370	O7 ... (n)fp	35.1±0.5	3.43±0.06	4.14±0.06	8.4	0.374	.
CYGOB2-4 A	O7 III ((f))	36.4±1.7	3.53±0.15	4.10±0.17	11.6	1.481	.
HD 93160 AB	O7 III ((f))	36.6±0.7	3.85±0.09	3.79±0.10	8.2	0.416	.
HD 24912	O7.5 III (n)((f))	35.9±0.5	3.67±0.04	3.94±0.05	4.1	0.278	.
HD 117797	O7.5 ... fp	33.8±1.1	3.33±0.09	4.18±0.11	9.7	0.743	.
HD 163800	O7.5 III ((f))	35.2±0.5	3.42±0.04	4.16±0.05	7.3	0.540	.
BD +60 261	O7.5 III (n)((f))	35.0±0.5	3.50±0.06	4.07±0.06	9.0	0.578	.
HD 186980	O7.5 III ((f))	35.8±0.5	3.48±0.04	4.13±0.05	7.5	0.357	.
HD 203064	O7.5 III n((f))	35.3±0.5	3.69±0.03	3.89±0.04	5.0	0.243	.
HD 97434	O7.5 III (n)((f))	34.8±0.5	3.57±0.07	3.99±0.07	8.2	0.434	.
HD 36861 A	O8 III ((f))	35.2±0.5	3.52±0.04	4.06±0.05	3.6	0.177	.

$$\mathcal{L} = T_{\text{eff}}^4 / g_{\text{true}}, \quad g_{\text{true}} = g + g_{\text{cent}}, \quad g_{\text{cent}} \approx \frac{(V_{\text{rot}} \sin i)^2}{R_*}$$

Table E.1: continued.

Name	SpT LC	T_{eff} [kK]	$\log g_{\text{true}}$ [dex]	$\log \mathcal{L}/\mathcal{L}_{\odot}$ [dex]	B [mag]	E(4405-5495)	Notes
HD 218195 A	O8.5 III Nstr	34.1±0.5	3.53±0.09	3.99±0.09	8.7	0.543	.
HD 114737 AB	O8.5 III	35.7±0.5	3.88±0.04	3.72±0.05	8.4	0.453	SB1
HD 116852	O8.5 II-III ((f))	34.0±0.5	3.52±0.04	4.00±0.05	8.4	0.148	.
HD 13268	ON8.5 III n	34.2±0.5	3.61±0.04	3.92±0.05	8.3	0.382	.
HD 150574	ON9 III (n)	33.1±0.9	3.60±0.10	3.87±0.11	8.7	0.492	.
HD 113904 B	O9 III	32.9±0.5	3.51±0.04	3.95±0.05	7.5	.	SB1
HD 305523	O9 II-III	32.2±0.5	3.44±0.05	3.98±0.06	8.6	0.397	.
HD 24431	O9 III	34.9±0.5	3.77±0.05	3.79±0.06	7.2	0.632	.
HD 193443 AB	O9 III	33.0±0.5	3.51±0.04	3.95±0.05	8.3	0.671	.
HD 105627	O9 III	33.7±0.6	3.63±0.08	3.87±0.09	8.2	0.305	SB1
HD 90087	O9.2 III (n)	31.6±0.6	3.50±0.07	3.89±0.08	7.8	0.263	.
HD 16832	O9.2 III	32.0±0.5	3.37±0.05	4.04±0.06	9.3	0.650	.
HD 152247	O9.2 III	32.1±0.5	3.48±0.06	3.94±0.07	7.6	0.455	SB1
HD 15642	O9.5 II-III n	29.9±0.8	3.52±0.04	3.77±0.06	8.6	0.306	.
HD 37737	O9.5 II-III (n)	30.0±0.5	3.50±0.03	3.80±0.04	8.4	0.566	SB1
HD 52266	O9.5 III n	32.2±0.8	3.63±0.09	3.79±0.10	7.2	0.244	.
HD 37743	O9.5 II-III (n)	30.8±0.5	3.33±0.04	4.01±0.05	3.5	0.044	.
HD 93521	O9.5 III nn	31.7±0.8	3.78±0.08	3.61±0.09	6.8	0.032	.
HD 117490	ON9.5 III nn	31.6±0.7	3.74±0.06	3.65±0.07	8.9	0.298	.
HD 91651	ON9.5 III n	31.8±0.8	3.56±0.06	3.84±0.07	8.8	0.252	SB1
HD 189957	O9.7 III	32.1±0.5	3.58±0.06	3.84±0.07	7.8	0.263	.
HD 154643	O9.7 III	31.0±0.5	3.51±0.04	3.85±0.05	7.4	0.507	SB1
HD 13022	O9.7 II-III	30.0±0.5	3.24±0.04	4.06±0.05	9.1	0.544	.
BD +60 498	O9.7 II-III	32.8±0.9	>3.99	<3.46	10.5	0.739	.
HD 118198	O9.7 III	31.2±0.5	3.42±0.04	3.95±0.05	8.7	0.400	.
HD 55879	O9.7 III	31.2±0.5	3.51±0.04	3.86±0.05	5.8	0.090	.
HD 64568	O3 V ((f*))z	46.9±1.0	3.93±0.06	4.14±0.07	9.5	0.373	Weak He I lines
HD 93128	O3.5 V ((fc))z	49.3±2.2	4.09±0.16	4.07±0.18	9.2	0.529	Weak He I lines
HD 93129 B	O3.5 V ((f))z	47.7±1.8	3.99±0.08	4.11±0.10	9.0	.	.
HD 5005 A	O4 V ((fc))	42.8±1.0	3.83±0.06	4.09±0.07	8.6	0.368	.
HD 164794	O4 V ((f))	43.1±1.1	3.88±0.07	4.05±0.08	6.5	0.315	.
HD 229232	O4 V: n((f))	42.9±2.2	3.81±0.09	4.11±0.13	10.4	1.141	Weak He I lines
HD 46223	O4 V ((f))	42.2±0.5	3.73±0.04	4.16±0.04	7.5	0.500	.
HD 93250 AB	O4 IV (fc)	45.0±0.6	3.86±0.05	4.14±0.06	7.9	0.454	.
HD 168076 AB	O4 IV (f)	43.0±1.8	3.92±0.15	4.00±0.17	9.2	0.736	.
HD 96715	O4 V ((f))z	45.2±1.2	3.91±0.12	4.10±0.13	8.4	0.399	.
HD 155913	O4.5 V n((f))	42.5±1.5	4.02±0.11	3.88±0.13	8.7	0.756	.
HD 192281	O4.5 IV (n)(f)	40.8±1.1	3.82±0.07	4.01±0.09	7.9	0.664	.
HD 193682	O4.5 IV (f)	41.0±1.0	3.75±0.10	4.09±0.11	8.9	0.774	.
HD 15629	O4.5 V ((fc))	41.8±0.5	3.79±0.05	4.08±0.05	8.8	0.704	.
HDE 303308 AB	O4.5 V ((fc))	41.1±0.9	3.90±0.08	3.95±0.09	8.6	0.455	.
HD 168112 AB	O5 IV (f)	39.7±1.0	3.71±0.13	4.08±0.14	9.9	0.948	SB1
HDE 319699	O5 V ((fc))	41.2±0.8	3.91±0.07	3.94±0.08	10.3	1.098	SB1
HD 46150	O5 V ((f))z	41.1±0.5	3.81±0.04	4.04±0.05	6.9	0.423	.
HD 256725 A	O5 V ((fc))	41.2±1.0	3.94±0.11	3.91±0.12	10.1	0.455	.
HD 305525	O5.5 V ((f))z	40.4±1.5	>3.89	<3.93	10.7	0.974	.
BD +60 134	O5.5 V (n)((f))	40.7±1.8	3.95±0.20	3.88±0.21	11.3	0.981	.
BD -14 5040	O5.5 V (n)((f))	40.4±2.3	3.96±0.23	3.86±0.25	11.5	1.285	Weak He I lines
HD 93204	O5.5 V ((f))	39.2±0.7	3.75±0.06	4.01±0.07	8.5	0.385	.
HD 14434	O5.5 IV nn(f)p	38.6±1.1	3.96±0.11	3.78±0.12	8.7	0.443	.
HDE 303311	O6 V ((f))z	40.1±0.7	3.91±0.06	3.89±0.07	9.1	0.414	.
HD 101190 AaAb	O6 IV ((f))	39.8±0.5	3.88±0.04	3.91±0.05	7.8	0.333	SB1
BD +60 2635	O6 V ((f))	39.8±0.9	3.77±0.10	4.02±0.11	10.6	0.715	.
ALS 4880	O6 V ((f))	39.8±1.2	3.96±0.20	3.83±0.21	11.3	1.137	.
CPD -58 2611	O6 V ((f))z	39.8±0.8	3.88±0.08	3.91±0.09	9.9	0.562	.
HD 42088	O6 V ((f))z	40.0±0.5	3.99±0.04	3.81±0.05	7.6	0.343	.
HD 76556	O6 IV (n)((f))p	37.9±0.5	3.90±0.08	3.80±0.08	8.6	0.678	.

$$\mathcal{L} = T_{\text{eff}}^4 / g_{\text{true}}, \quad g_{\text{true}} = g + g_{\text{cent}}, \quad g_{\text{cent}} \approx \frac{(V_{\text{rot}} \sin i)^2}{R_*}$$

Table E.1: continued.

Name	SpT LC	T_{eff} [kK]	$\log g_{\text{true}}$ [dex]	$\log \mathcal{L}/\mathcal{L}_{\odot}$ [dex]	B [mag]	E(4405-5495)	Notes
CPD-592600	O6 V ((f))	39.3±0.8	3.86±0.08	3.91±0.09	8.8	0.507	SB1
BD +62 424	O6.5 V (n)((f))	38.7±0.7	3.80±0.10	3.94±0.10	9.3	0.717	.
HD 101298	O6.5 IV ((f))	38.9±0.5	3.79±0.04	3.96±0.05	8.1	0.355	.
HD 199579	O6.5 V ((f))z	39.5±0.8	3.86±0.07	3.92±0.08	6.0	0.342	SB1
HD 99897	O6.5 IV ((f))	37.7±0.5	3.57±0.04	4.13±0.05	8.5	0.434	.
HD 242935 A	O6.5 V ((f))z	38.7±0.9	>3.98	<3.76	9.8	0.503	.
HDE 227018	O6.5 V ((f))z	38.7±0.8	3.85±0.15	3.89±0.15	9.4	0.683	.
HD 305532	O6.5 V ((f))z	39.3±0.8	3.84±0.07	3.93±0.08	10.5	0.613	.
BD +61 411	O6.5 V ((f))z	38.8±1.0	3.99±0.18	3.76±0.19	11.2	1.315	.
HD 93161 B	O6.5 IV ((f))	37.1±0.8	3.76±0.12	3.91±0.13	8.7	0.530	.
HD 344784	O6.5 V ((f))z	38.9±0.6	3.90±0.06	3.85±0.07	9.9	0.831	.
HD 228841	O6.5 V n((f))	37.7±1.4	3.88±0.13	3.82±0.15	9.5	0.833	.
HDE 322417	O6.5 IV ((f))	38.6±0.8	3.74±0.10	4.00±0.11	10.9	1.112	.
HD 91572	O6.5 V ((f))z	38.8±0.5	3.84±0.08	3.91±0.08	8.3	0.359	.
HD 167633	O6.5 V ((f))	38.0±0.8	3.72±0.07	3.99±0.08	8.4	0.525	SB1
HD 12993	O6.5 V ((f)) Nstr	39.2±0.6	3.89±0.07	3.87±0.07	9.2	0.464	.
ALS 12370	O6.5 V nn((f))	39.0±1.8	4.12±0.20	3.63±0.22	10.5	0.486	.
HD 326775	O6.5 V (n)((f))z	39.4±1.3	3.87±0.14	3.90±0.15	11.6	1.276	SB1
BD -10 4682	O7 V n((f))	36.9±1.2	3.94±0.11	3.72±0.12	10.2	0.774	.
HD 5689	O7 V n((f))	36.8±1.0	3.72±0.10	3.93±0.11	9.5	0.591	.
HD 46485	O7 V ((f))n var?	36.1±0.7	3.88±0.04	3.74±0.05	8.6	0.579	.
HD 36879	O7 V (n)((f))	36.9±0.5	3.77±0.04	3.89±0.05	7.8	0.464	.
HD 217086	O7 V nn((f))z	37.7±0.8	4.00±0.07	3.70±0.08	8.3	0.884	.
BD +60 513	O7 V n	35.8±1.0	3.86±0.10	3.75±0.11	9.9	0.756	.
HDE 227465	O7 V ((f))	37.2±1.0	3.87±0.15	3.80±0.16	10.7	0.738	.
HD 90273	ON7 V ((f))	38.5±0.8	3.78±0.10	3.95±0.11	9.2	0.437	.
BD +62 2078	O7 V ((f))z	38.7±0.8	4.00±0.14	3.74±0.14	10.8	1.362	.
HD 46573	O7 V ((f))z	36.8±0.8	3.72±0.10	3.93±0.11	8.3	0.613	.
HD 44811	O7 V (n)z	37.4±0.6	3.90±0.11	3.78±0.11	8.6	0.428	.
HD 159176	O7 V ((f))	37.6±0.6	3.83±0.10	3.86±0.10	5.8	0.314	.
HD 47839	O7 V ((f))z var	38.3±0.5	4.02±0.05	3.70±0.05	4.6	0.054	.
ALS 8294	O7 V (n)z	41.7±1.9	3.97±0.21	3.90±0.22	10.7	0.789	.
BD +60 501	O7 V (n)((f))z	37.9±0.8	3.89±0.11	3.81±0.12	10.1	0.709	.
BD +60 586	O7 V z	38.4±0.7	4.10±0.13	3.63±0.13	8.8	0.584	.
HD 193595	O7 V ((f))	37.9±0.5	3.79±0.06	3.91±0.06	9.1	0.640	.
HDE 227245	O7 V ((f))z	38.0±0.7	3.80±0.07	3.91±0.08	10.3	0.878	.
HD 152623	O7 V (n)((f))	37.4±0.7	3.79±0.10	3.89±0.11	7.5	0.374	SB1
ALS 12619	O7 V ((f))z	38.2±0.7	4.03±0.08	3.69±0.09	11.3	0.752	.
HD 110360	ON7 V	39.3±0.9	4.17±0.14	3.60±0.15	9.5	0.458	SB1
HD 93222 AB	O7 V ((f))	36.8±0.7	3.63±0.11	4.02±0.11	8.8	0.329	.
HD 91824	O7 V ((f))z	39.8±0.9	4.02±0.13	3.77±0.14	8.1	0.233	SB1
HD 93146 A	O7 V ((f))	38.7±0.6	3.84±0.07	3.90±0.08	8.4	0.296	SB1
HDE 242926	O7 V z	39.0±0.7	4.07±0.11	3.68±0.11	9.7	0.614	.
HD 53975	O7.5 V z	36.8±0.5	3.91±0.06	3.74±0.06	6.4	0.194	SB1
HD 168504	O7.5 V (n)z	37.3±0.7	3.84±0.07	3.84±0.08	9.7	0.709	.
HDE 344777	O7.5 V z	35.8±0.8	3.62±0.12	3.99±0.13	10.2	1.045	.
HDE 338 916	O7.5 V z	37.8±0.8	4.02±0.12	3.68±0.13	10.8	0.898	.
HD 168461	O7.5 V ((f)) Nstr	36.0±1.2	3.81±0.16	3.81±0.17	10.2	0.907	.
HD 164492	O7.5 V z	38.6±0.6	4.00±0.10	3.74±0.10	7.6	0.286	.
BD +33 1025 A	O7.5 V (n)z	38.4±1.0	>4.01	<3.72	10.7	0.540	.
HD 124979	O7.5 IV (n)((f))	34.9±0.9	3.58±0.05	3.98±0.07	8.6	0.342	.
HD 152590	O7.5 V z	38.0±0.5	3.92±0.07	3.79±0.07	8.6	0.419	SB1
HD 35619	O7.5 V ((f))	37.7±0.6	3.94±0.12	3.76±0.12	8.8	0.529	.
HD 74920	O7.5 IV n((f))	34.9±0.5	3.66±0.05	3.90±0.06	7.6	0.306	.
HD 41997	O7.5 V n((f))	35.8±0.5	3.75±0.05	3.86±0.06	8.8	0.661	SB1
HD 99546	O7.5 V ((f)) Nstr	37.0±0.5	3.71±0.05	3.95±0.06	8.2	0.249	.
HD 94024	O8 IV	34.8±0.5	3.56±0.05	4.00±0.06	8.8	0.411	SB1

$$\mathcal{L} = T_{\text{eff}}^4 / g_{\text{true}}, \quad g_{\text{true}} = g + g_{\text{cent}}, \quad g_{\text{cent}} \approx \frac{(V_{\text{rot}} \sin i)^2}{R_*}$$

Table E.1: continued.

Name	SpT LC	T_{eff} [kK]	$\log g_{\text{true}}$ [dex]	$\log \mathcal{L}/\mathcal{L}_{\odot}$ [dex]	B [mag]	E(4405-5495)	Notes
HD 101413	O8 V	36.9±0.5	4.01±0.07	3.65±0.07	8.6	0.376	.
HD 165246	O8 V (n)	35.9±0.7	3.99±0.07	3.62±0.08	7.9	0.379	SB1
HD 41161	O8 V n	35.2±0.6	3.84±0.05	3.74±0.06	6.7	0.207	.
HD 46056	O8 V n	35.5±0.8	4.01±0.09	3.58±0.10	8.4	0.468	.
HD 326331	O8 IV n((f))	34.9±0.5	3.74±0.04	3.82±0.05	7.6	0.499	.
HD 101191	O8 V	35.7±0.9	3.80±0.12	3.80±0.13	8.5	0.338	.
HD 135591	O8 IV ((f))	35.0±0.5	3.58±0.04	3.99±0.05	5.4	0.203	.
HD 191978	O8 V	35.8±0.6	3.81±0.08	3.80±0.09	8.2	0.417	.
HD 101223	O8 V	35.2±0.5	3.62±0.05	3.96±0.06	8.9	0.456	.
HD 97848	O8 V	35.6±0.6	3.67±0.06	3.93±0.07	8.7	0.286	.
ALS 7833	O8 Vz	35.9±1.2	3.71±0.13	3.90±0.14	10.4	0.542	.
HD 5005 C	O8.5 V (n)	36.2±0.6	4.04±0.08	3.58±0.09	8.9	.	.
Trumpler 14-9	O8.5 V	36.7±0.7	4.10±0.11	3.55±0.11	10.1	0.455	.
HD 46149	O8.5 V	36.9±0.5	4.23±0.08	3.43±0.08	7.8	0.439	.
HDE 298429	O8.5 V	33.6±1.1	3.55±0.14	3.95±0.15	10.3	0.847	.
HD 46966	O8.5 IV	35.9±0.5	3.84±0.07	3.77±0.07	7.1	0.254	.
BD +36 4145	O8.5 V (n)	35.8±0.9	3.86±0.15	3.75±0.16	9.6	0.919	.
HD 92504	O8.5 V (n)	34.9±0.8	3.70±0.04	3.86±0.06	8.4	0.240	.
HD 52533	O8.5 IV n	35.2±0.5	3.98±0.05	3.60±0.06	7.6	0.194	SB1
HD 216532	O8.5 V (n)	35.3±0.6	4.04±0.07	3.54±0.08	8.5	0.815	.
HD 73882	O8.5 IV	35.8±0.6	3.85±0.10	3.76±0.10	8.0	0.665	SB1
HD 48279	O8.5 V Nstr var?	36.2±0.7	3.86±0.06	3.76±0.07	8.0	0.413	.
HD 14633 AaAb	ON8.5 V	35.0±0.5	3.79±0.08	3.78±0.08	7.2	0.071	SB1
HD 214680	O9 V	35.2±0.5	3.89±0.04	3.69±0.05	4.7	0.077	.
HD 102415	ON9 IV: nn	33.1±1.1	3.92±0.10	3.55±0.12	9.4	0.394	.
HD 149452	O9 IV n	33.7±0.8	3.73±0.07	3.77±0.08	9.6	0.850	.
HD 93028	O9 IV	35.3±0.7	3.93±0.08	3.65±0.09	8.3	0.203	SB1
CPD -59 2551	O9 V	34.9±0.5	3.91±0.05	3.65±0.06	9.2	0.267	.
HD 216898	O9 V	35.9±0.6	4.18±0.11	3.43±0.11	8.5	0.794	SB1
HD 12323	ON9.2 V	34.2±0.9	3.95±0.18	3.58±0.19	8.8	0.238	SB1
HD 46202	O9.2 V	34.9±0.5	4.13±0.07	3.43±0.07	8.7	0.462	.
HD 57682	O9.2 IV	35.0±0.5	4.13±0.14	3.44±0.14	6.2	0.087	.
HD 76341	O9.2 IV	33.0±0.5	3.57±0.08	3.89±0.08	7.5	0.579	.
HD 164438	O9.2 IV	32.2±0.5	3.43±0.04	3.99±0.05	7.8	0.587	SB1
HD 201345	ON9.2 IV	33.8±0.7	3.79±0.06	3.72±0.07	7.6	0.149	.
HD 5005 D	O9.2 V	34.9±0.5	3.99±0.09	3.57±0.09	9.7	0.318	.
HD 96622	O9.2 IV	33.3±0.6	3.68±0.11	3.80±0.11	9.1	0.424	SB1
HD 149757	O9.2 IV nn	32.0±0.5	3.66±0.04	3.75±0.05	2.6	0.297	.
HD 163892	O9.5 IV (n)	32.8±0.5	3.77±0.05	3.68±0.06	7.6	0.407	SB1
HD 166546	O9.5 IV	32.4±0.6	3.56±0.08	3.87±0.09	7.3	0.301	.
CPD -54 6791	O9.5 V	34.8±0.6	4.05±0.10	3.51±0.10	11.5	0.796	.
HD 34078	O9.5 V	34.5±0.8	4.07±0.14	3.47±0.15	6.2	0.489	.
HD 38666	O9.5 V	33.9±0.5	3.92±0.04	3.59±0.05	4.9	0.016	.
HD 36483	O9.5 IV (n)	33.4±0.8	3.86±0.11	3.62±0.12	8.6	0.676	.
HD 206183	O9.5 IV-V	33.8±0.5	4.04±0.09	3.47±0.09	7.5	0.383	.
HD 202214	O9.5 IV	32.1±0.5	3.82±0.04	3.60±0.05	6.6	0.379	.
HD 168941	O9.5 IV p	32.0±0.5	3.43±0.05	3.98±0.06	9.4	0.310	.
HD 155889 AB	O9.5 IV	34.9±0.7	4.10±0.07	3.46±0.08	7.0	0.237	.
HD 164019	O9.5 IV p	32.0±0.5	3.45±0.07	3.96±0.08	9.5	0.495	.
HD 123056	O9.5 IV (n)	31.8±0.5	3.70±0.07	3.70±0.08	8.3	0.385	SB1
BD +60 499	O9.5 V	34.2±0.8	3.87±0.12	3.66±0.13	10.8	0.794	.
HD 93027	O9.5 IV	33.8±0.5	3.95±0.07	3.56±0.07	8.7	0.229	.
HD 192001	O9.5 IV	33.0±0.5	3.83±0.05	3.63±0.06	8.6	0.566	.
HDE 308813	O9.7 IV (n)	31.8±0.5	3.88±0.05	3.52±0.06	9.3	0.295	SB1
CPD -41 7721 A	O9.7 V: (n)	31.3±0.5	3.85±0.09	3.52±0.09	8.8	0.394	.
HDE 326329	O9.7 V	32.1±0.5	3.92±0.05	3.50±0.06	8.8	0.402	.
HD 36512	O9.7 V	33.0±0.5	4.02±0.09	3.44±0.09	4.4	0.022	.

$$\mathcal{L} = T_{\text{eff}}^4 / g_{\text{true}}, \quad g_{\text{true}} = g + g_{\text{cent}}, \quad g_{\text{cent}} \approx \frac{(V_{\text{rot}} \sin i)^2}{R_*}$$

Table E.1: continued.

Name	SpT LC	T_{eff} [kK]	$\log g_{\text{true}}$ [dex]	$\log \mathcal{L}/\mathcal{L}_{\odot}$ [dex]	B [mag]	E(4405-5495)	Notes
HD 209339	O9.7 IV	32.1±0.5	3.81±0.04	3.61±0.05	6.8	0.314	.
HD 54879	O9.7 V	33.5±0.5	4.09±0.11	3.40±0.11	7.6	0.269	.
HD 152200	O9.7 IV (n)	30.4±0.7	3.69±0.11	3.63±0.12	8.4	0.387	SB1
HD 207538	O9.7 IV	32.0±0.5	3.80±0.04	3.61±0.05	7.6	0.569	.

$$\mathcal{L} = T_{\text{eff}}^4 / g_{\text{true}}, \quad g_{\text{true}} = g + g_{\text{cent}}, \quad g_{\text{cent}} \approx \frac{(V_{\text{rot}} \sin i)^2}{R_*}$$

Table E.2: 113 O-type stars in the sample with double-line spectroscopic features, separated by luminosity class (I+II, III, and IV+V) and sorted by spectral type. No analysis available. It details name, approximate spectral classification (sometimes is known to be a compromise, as the case of HD 37468, an SB3 star Simón-Díaz et al. 2015b; Maíz Apellániz et al. 2018), B magnitude, reddening parameter $E(4405-5495)$, and secondary component spectral classification in the unresolved spectrum. Everything listed in GOSC (Maíz Apellániz et al. 2013) and Maíz Apellániz & Barbá (2018).

Name	SpT LC	B [mag]	$E(4405-5495)$	LC comp.
HD 93162	O2.5 I f*/WN6	8.5	0.695	OB
LS III +4611	O3.5 I f*	12.5	1.726	O3.5If*
HD 228 766	O4 I f*	9.8	0.884	O8:II:
HDE 229196	O6 II (f)	9.4	1.158	.
HD 153919	O6 Ia fcp	6.8	0.499	.
HD 150958	O6.5 Ia (n)f	7.9	0.613	.
HD 152248	O7 Iab f	6.3	0.403	O7Ib(f)
HD 101205	O7 II: (n)	6.6	0.322	.
HD 57060	O7 Ia fp var	4.8	0.131	.
HD 166734	O7.5 Iab f	9.5	1.284	.
HD 167971	O8 Ia f(n)	8.9	0.986	O4/5
HD 149404	O8.5 Iab (f)p	5.9	0.621	.
HD 57061 AaAb	O9 II	4.8	0.103	.
HD 323110	ON9 Ia	10.9	1.474	.
HD 1337	O9.2 II	6	0.140	O8V((f))
HD 35921	O9.5 II	7.3	0.425	O9III
HD 69106	O9.7 II n	7	0.214	.
HD 93206	O9.7 Ib n	7	0.342	.
HD 17505	O6.5+O8 III+V n(f)+...	7.7	0.636	.
HD 150136	O3.5-4 III (f*)	6.1	0.443	O6IV
HD 191201	O9.5+O9.7 III+III ...+...	7.8	0.401	B0IV
HD 124314	O6+O9.2 IV+IV (n)((f))+ (n)	7.5	0.457	.
HDE 319718 A	O3.5 III (f*)	12.8	1.814	.
HD 15558	O4.5 III (f)	8.4	0.747	.
HD 93403	O5.5 III (fc) var	7.5	0.503	.
HD 93130	O6.5 III (f)	8.4	0.501	.
HD 167771	O7 III ((f))	6.6	0.360	O8III
HD 115455	O8 III ((f))	8.2	0.472	.
HDE 319702	O8 III	11	1.206	.
HD 47129	O8 ... fp var	6.1	0.331	.
HD 96670	O8.5 ... (n)fp var	7.9	0.444	.
HD 151003	O8.5 III	7.6	0.436	.
HD 153426	O8.5 III	7.6	0.392	.
HD 19820	O8.5 III (n)((f))	7.6	0.763	.
HD 114886	O9 III	7.5	0.376	O9.5III
HD 16429	O9 II-III (n) Nwk	8.5	0.842	.
HD 37043	O9 III var	2.6	0.042	.
HD 93249 A	O9 III	8.5	0.382	.
HD 15137	O9.5 II-III n	7.9	0.283	.
HD 167263	O9.5 III	6.1	0.268	.
HD 152219	O9.5 III (n)	7.8	0.416	.
HD 96264	O9.5 III	7.5	0.203	.
HD 156292	O9.7 III	7.8	0.502	B
HD 155775	O9.7 III (n)	6.7	0.243	.
HD 46106	O9.7 III (n)	8.1	0.392	.
HD 37468 AB	O9.7 III	4.4	0.032	.
HD 117856	O9.7 II-III	7.6	0.433	.
HD 93205	O3.5 V ((f))	7.8	0.351	O8V
LS III +4612	O4.5 IV (f)	11.4	1.323	.
HD 242908	O4.5 V (n)((fc))z	9.3	0.561	.
BD +45 3216 A	O5 V ((f))z	10	0.685	.
HD 48099	O5.5 V ((f))z	6.3	0.243	O9V

Table E.2: continued.

Name	SpT LC	<i>B</i> [mag]	E(4405-5495)	LC comp.
V747 CEP	O5.5 V (n)((f))	11.4	1.641	.
ALS 12688	O5.5 V (n)((fc))	11.3	0.860	B
BD -16 4826	O5.5 V ((f))z	10.6	1.032	.
HD 64315	O5.5 V	10.1	0.507	O7V
HD 215835	O5.5 V ((f))	8.9	0.614	O6V((f))
HD 101131	O5.5 V ((f))	7.4	0.319	O8:V
MY CAM	O5.5 V (n)	10	0.565	O6.5V(n)
HD 165052	O6 V z	7	0.392	O8Vz
HDE 228 854	O6 IV n var	9.5	0.921	O5Vnvar
HD 92206 A	O6 V ((f))z	8.3	0.406	.
CPD -59 2641	O6 V ((fc))	9.5	0.603	.
HD 92206 B	O6 V ((f))	9.3	0.428	.
HD 168075	O6.5 V ((f))	9.2	0.752	.
HD 194649 AB	O6.5 V ((f))	10.6	1.260	.
HD 150135	O6.5 V ((f))z	7.5	0.447	.
HDE 228 759	O6.5 V (n)((f))z	10.1	1.002	.
HD 18326	O6.5 V ((f))z	8.3	0.636	O9/B0V:
HD 206267	O6.5 V ((f))	6.2	0.504	O9/B0V
HD 101436	O6.5 V ((f))	7.7	0.354	.
BD +60 497	O6.5 V ((f))	9.4	0.835	O8/B0V
Herschel 36	O7: V	11	0.825	.
HD 175514	O7 V (n)((f))z	9.2	0.848	B
ALS 12320	O7 IV ((f))	11.2	0.996	.
ALS 8272	O7 V ((f))	11.8	0.788	B0III-V
HD 135240	O7 IV ((f))	5.2	0.208	B
HD 54662	O7 V z var?	6.8	0.305	.
HD 165921	O7 V (n)z	7.5	0.411	B0:V:
HD 319703 A	O7 V ((f))	11.9	1.476	O9.5V
HD 213023 A	O7.5 V z	9.9	1.071	.
HDE 229 202	O7.5 V (n)((f))	10.4	1.188	.
HD 93161 A	O7.5 V	8.6	.	O9V
BD -14 5014	O7.5 V (n)((f))	11.1	0.921	.
HD 97166	O7.5 IV ((f))	8	0.351	O9III:
V572 CAR	O7.5 V (n)	8.9	0.431	B0V(n)
BD +66 1675	O7.5 V z	10.1	1.403	.
BD +55 2840	O7.5 V (n)	10.6	0.771	.
HD 161853	O8 V (n)z	8.1	0.496	B
HD 100213	O8 V (n)	8.4	0.340	B0V(n)
CPD -59 2635	O8 V (n)	9.5	0.534	O9.5V
HD 17520	O8 V	9.1	0.589	.
HD 123590	O8 V z	8.4	0.418	.
HD 92206 C	O8 V (n)z	9.1	0.424	B0:V
CPD -59 2636	O8 V	10.1	0.637	O8V
HD 93343	O8 V	9.8	0.524	.
HD 168137 AaAb	O8 V z	10	0.678	.
HD 57236	O8.5 V	8.9	0.475	.
CPD -41 7733	O9 IV	7.9	0.441	.
HD 193322	O9 IV (n)	6.8	0.381	.
HD 75759	O9 V	6.1	0.185	B0V
HD 152218	O9 IV	7.8	0.454	B0:V:
HD 152314	O9 IV	8.2	0.493	.
HD 152246	O9 IV	8.1	0.428	.
HD 209481	O9 IV (n) var	5.6	0.326	B1:V:
HD 158186	O9.2 V	7.1	0.291	B1:V
HD 37366	O9.5 IV	7.7	0.365	.
HD 204827	O9.5 IV	9.3	1.072	.
HD 115071	O9.5 III	8.2	0.489	B0Ib
HD 164816	O9.5 V	7.1	0.258	B0V

Table E.2: continued.

Name	SpT LC	B [mag]	E(4405-5495)	LC comp.
HD 37041	O9.5 IV p	5	0.200	.
HD 198846	O9.5 IV	7.2	0.183	O9.5IV
HD 125206	O9.7 IV n	8.5	0.487	.

Table E.3: 17 peculiar stars (Oe, WR, and Mag) in the sample with no spectroscopic analysis available, separated by luminosity class (I+II, III, and IV+V) and sorted by spectral type. Columns include: name, spectral class, B magnitude, reddening parameter $E(4405-5495)$, and the reason that makes the analysis of the star impossible, i.e., the star is Oe, Magnetic or WR. Magnetic stars include reference to its magnetic detection.

Name	SpT LC	B [mag]	$E(4405-5495)$	Notes Notes
HD 66811	O4 I(n)fp	2	0.012	Mag*
ALS 2063	O5 Ifp	11.5	1.027	WR
HD 152386	O6: Ia fpe	8.6	0.775	WR
HD 313846	O7: Ia fpe	10.7	1.113	WR
HD 152408	O8: Ia fpe	5.9	0.414	WR
HD 226868	O9.7 Iab p var	9.7	1.042	Mag**
HD 148937	O6 ... f?p	7.8	0.619	Mag***
CPD -28 2561	O6.5 . f?p	10.1	0.439	Mag****
HD 108	O8 ... fp var	7.5	0.434	Mag ^o
HD 191612	O8 ... f?p var	8	0.532	Mag ^{o*}
HD 45314	O9: ... npe	6.7	.	Oe
HD 24534	O9.5: ... npe	7.1	.	Oe
HD 39680	O6 V: [n]pe var	7.9	.	Oe
HD 37022	O7 V p	5.2	0.286	Mag ^{o***}
HD 155806	O7.5 V ((f))(e)	6.1	.	Oe
HD 60848	O8: V: pe	6.7	.	Oe
HD 120678	O9.5 V e	8.1	.	Oe

Notes: Mag:Magnetic, WR: Wolf-Rayet.

*: Grunhut et al. (2017), **: Caballero-Nieves et al. (2009).

: Hubrig et al. (2008),*: Hubrig et al. (2011), ^o: Martins et al. (2010).

^{o*}: Wade et al. (2011), ^{o**}: Nazé et al. (2008).